Transient grating excitation of phonon-polaritons in a $LiNbO_3$ waveguide

by Johannes Müller

Submitted to the Institute of physics and astronomy
of the University of Potsdam

A thesis presented for the degree of
Bachelor of Science

Supervisor : Alexander von Reppert
First assessor : Prof. Dr. Matias Bargheer
Second assessor : Prof. Dr. Markus Gühr

August 13, 2021

Abstract

In this work, I present experiments with a transient grating setup, that employs a four-wave mixing process to selectively excite and detect phonon-polaritons. The phonon-polaritons arise due to a strong coupling between electromagnetic terahertz radiation and transverse optical phonons in ionic crystals. The occurrence of this coupling requires phonon modes that are both Raman and infrared active. The ferroelectric material $LiNbO_3$ was investigated due to its strong Raman and infrared active transverse optical phonon modes.

I examined two samples of different thicknesses, a one millimeter thick bulk and a 50 micrometer thin waveguide specimen of x-cut $LiNbO_3$. Phonon-polaritons excited in bulk $LiNbO_3$ have been studied previously in greater detail in our group. As a part of this work, I rebuilt the setup used for these studies and investigated the waveguide. I observe and rationalize the more complex time-dependent diffraction signal in the waveguide by the superposition of multiple waveguide modes. They arise due to the additional confinement of the phonon-polariton modes along the out-of-plane direction in the thin dielectric slab. In this work, three transverse magnetic waveguide modes are excited, and their properties compared to a theoretical prediction.

The impact of homodyne detection effects on the detected diffraction signal is compared for the two samples using a systematic variation of the excitation fluence. For the bulk, a second peak in the Fourier analysis at twice the actual frequency of the wave packets is apparent for high excitation fluences due to superimposed left and right propagating phonon-polaritons. In the waveguide this does not occur, and only the three waveguide modes are excited as predicted and simulated in the theory part of this thesis.

Rotation of the c-axis of the sample with respect to the polarization of the excitation pulses leads to a strong decrease of the amplitude of the oscillations caused by the phonon-polaritons and a blue-shift in the observed frequencies. A displacement series of the probe beam with respect to the pump region follows the propagating wave packets up to a displacement distance of 1.5 mm. Higher order waveguide modes are found to be damped so that at large displacements only the zeroth transverse magnetic mode is apparent. The group refractive index of n_{group}=7.83 for the $LiNbO_3$ waveguide is determined and coincides to previous investigations in $LiNbO_3$.

This work is the first time phonon-polariton waveguide modes have been studied in our group. They may become useful in future experiments, since their confinement to the near surface region may allow for a coupling of the tunable evanescent THz waves to excitations in materials that can be placed next to the waveguide.

Zusammenfassung

In dieser Arbeit stelle ich Experimente mit einem transienten Gitteraufbau vor, bei dem ein vier-Wellen-Mischprozess zur selektiven Anregung und zum Nachweis von Phonon-Polaritonen verwendet wird. Die Phonon-Polaritonen entstehen durch eine starke Kopplung zwischen elektromagnetischer Terahertz-Strahlung und transversalen optischen Phononen in ionischen Kristallen. Für diese Kopplung sind Phononenmoden erforderlich, die sowohl Raman- als auch infrarotaktiv sind. Das ferroelektrische Material $LiNbO_3$ wurde aufgrund seiner starken Raman- und infrarotaktiven transversalen optischen Phononmoden untersucht.
Ich untersuchte zwei unterschiedlich dicke Proben, eine einen Millimeter dicke Bulk-Probe und eine 50 Mikrometer dünne Wellenleiterprobe aus x-cut $LiNbO_3$. Phonon-Polaritonen, die in $LiNbO_3$ angeregt werden, wurden in unserer Gruppe bereits ausführlich untersucht. Im Rahmen dieser Arbeit habe ich den für diese Studien verwendeten Aufbau umgebaut und den Wellenleiter untersucht. Ich beobachte und erkläre das komplexere zeitabhängige Beugungssignal im Wellenleiter durch die Überlagerung mehrerer Wellenleitermoden. Sie entstehen durch den zusätzlichen Einschluss der Phonon-Polariton-Moden entlang der Richtung senkrecht zur Probenebene in der dünnen dielektrischen Platte. In dieser Arbeit werden drei transversale magnetische Wellenleitermoden angeregt und ihre Eigenschaften mit einer theoretischen Vorhersage verglichen.
Die Auswirkungen von homodynen Detektionseffekten auf das aufgenommene Beugungssignal werden für die beiden Proben unter Verwendung einer systematischen Variation der Anregungsfluenz verglichen. Für die Masse ist bei hohen Anregungsfluenzen ein zweiter Peak in der Fourier-Analyse bei der doppelten Frequenz der Wellenpakete zu erkennen, der auf überlagerte links- und rechtspropagariende Phonon-Polaritonen zurückzuführen ist. Im Wellenleiter tritt dies nicht auf und nur die drei Wellenleitermoden werden angeregt, wie im Theorieteil dieser Arbeit vorhergesagt und simuliert wurde.
Eine Drehung der c-Achse der Probe in Bezug auf die Polarisation der Anregungspulse führt zu einer starken Abnahme der Amplitude der durch Phonon-Polaritonen verursachten Oszillationen und zu einer Blauverschiebung der beobachteten Frequenzen. Eine Verschiebungsreihe des Abfragestrahls in Bezug auf den Anregungsbereich folgt den sich ausbreitenden Wellenpaketen bis zu einem Verschiebungsabstand von 1.5 mm. Es wurde festgestellt, dass Wellenleitermoden höherer Ordnung gedämpft werden, sodass bei großen Auslenkungen nur die nullte transversale magnetische Mode auftritt. Der Gruppenbrechungsindex von n_{group}=7.83 für den $LiNbO_3$-Wellenleiter wurde bestimmt und stimmt mit früheren Untersuchungen in $LiNbO_3$ überein. Diese Arbeit ist das erste Mal, dass Phonon-Polariton-Wellenleitermoden in unserer Gruppe untersucht wurden. Sie könnten sich in zukünftigen Experimenten als nützlich erweisen, da ihre Bindung zum oberflächennahen Bereich eine Kopplung der durchstimmbaren evaneszenten THz-Wellen mit Anregungen in Materialien ermöglichen könnte, die auf oder neben dem Wellenleiter angeordnet werden können.

Contents

List of Figures

List of Tables

1. Introduction and theoretical background

The continuing development of signal processing and telecommunication leads to a continuation of miniaturization of switching circuits in micro- and nanoelectronics. Simultaneously, the speed of data evolve up to high frequency electronics at 100 GHz and low frequency optics in the region above 10 THz. High-bandwidth signal processing in the terahertz range, THz imaging and spectroscopy are driven by the development of femtoseconds laser-based methods to generate THz pulses [1], [2], [3].
In terahertz polaritonics the transport of the signal is carried by the quasiparticles phonon-polaritons, a mixture of electromagnetic radiation and a vibrational mode of a polar dielectric medium, that propagate through the sample at light-like speed and are a source of intense ultra-short terahertz radiation [4]. One approach to excite THz phonon-polaritons is impulsive stimulated Raman scattering (ISRS), a second order non-linear process. Since the first investigations of phonon-polaritons in the sixties [5] the guidance, processing, characterization and interference has been an active field of research. Ferroelectric materials are often used as samples since they contain modes in the far-infrared frequency region, which are both optical Raman and infrared active [6].
One approach to selectively excite and detect electromagnetic waves in the terahertz region is the transient grating setup [7], whose (re-)construction was part of this work. A transient grating setup is used in fundamental and applied research [8], [9]. When two coherent pulses are crossed in the sample as shown in Fig.1.1 an interference pattern is induced with a spatial period depending on the intersection angle of the crossed pulses in air Θ_{air}. The interference pattern defines a spatial period that excites quasiparticles in the sample with the corresponding wave vector, this process can be described as a four-wave mixing process. This thesis examines the properties of two samples of different thickness, consisting of x-cut lithium niobate ($LiNbO_3$). I discuss different types of measurements and compare the response of bulk with a thickness of 1 mm and a slab waveguide specimen with a thickness of 50 μm. Phonon-polaritons in bulk $LiNbO_3$ travel into the bulk, but they are confined to the near surface region in the waveguide. This might be advantageous in further studies on the propagation and coupling of phonon-polaritons of the group. To rationalize the occurrence of additional waveguide modes that result from the confinement requires a more advanced discussion of the phonon-polariton dispersion of $LiNbO_3$. [10], [11].
This thesis is structured as follows: Chapter 1 presents the motivation and necessary theoretical background required to understand the implemented experiments. Chapter 2 presents the description of the experimental setup and data analysis routine. Chapter 3 discusses the results. The focus is on the comparison of the recorded data between the bulk and slab waveguide. This thesis discusses the fluence-dependent excitation of phonon-polaritons and emphasizes the importance of the orientation of the optical axis of the ferroelectric sample with respect to the polarization of the excitation pulses. The propagation of phonon-polariton wave packets in the bulk and the waveguide is analyzed. Chapter 4 provides a summary of the findings and an outlook on possible further experiments. An appendix contains mathematical derivations that would otherwise obstruct the flow of arguments.

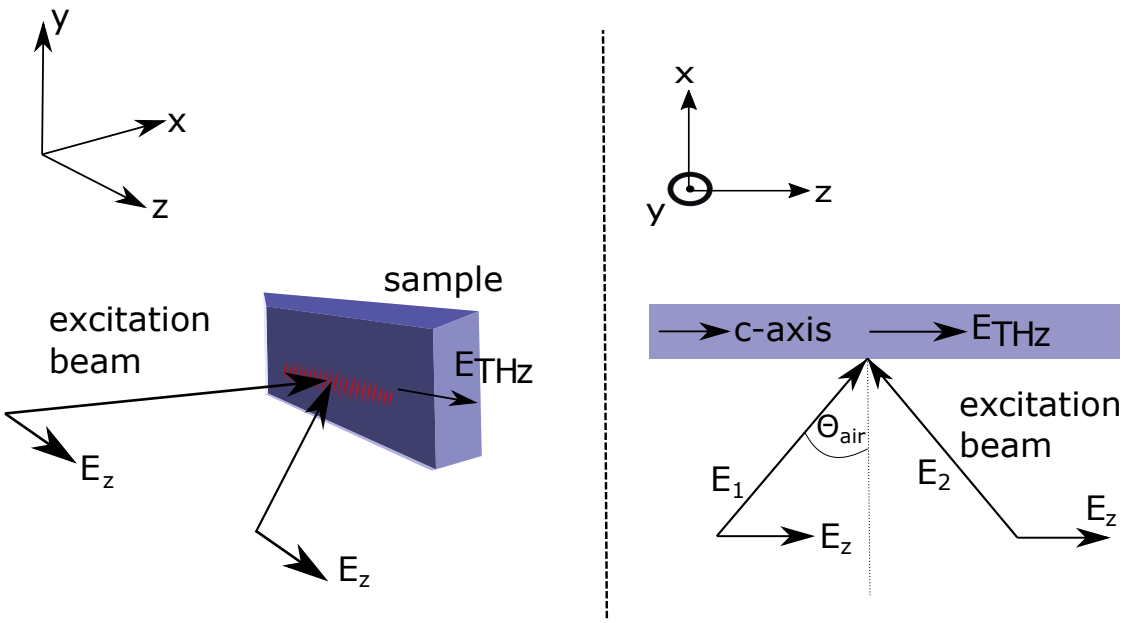

Figure 1.1.: Side and top view of the configuration of the excitation of the sample

1.1. Phonon-polaritons

Generally speaking, the quasiparticle that describes the coupling between an excited state, usually charged particles and electromagnetic waves, is called a polariton. The dispersion of this quasiparticle was introduced first by Kun Huang in 1951 [12]. Various excited states and its origins result in different quasiparticles, e.g. the coupling with spin waves in ferroelectric samples are indicated as magnon-polaritons [13], the coupling with collective electron vibrations that are known as plasmon-polaritons or coupling with transverse optical phonon in a polar lattice, commonly called phonon-polariton which is described furthermore in the following.
Vibrational excitations in crystals are well approximated by the harmonic oscillator model. Their eigenfrequencies are determined by the material specific interatomic interactions. The energy quanta of this excitation are called phonons, which are described in standard textbooks [14], [15]. When a transverse optical phonon is excited in an ionic structure, the oscillating ions act as dipoles which emit electromagnetic radiation. By stimulating various neighboring ions within a few femtoseconds, the oscillations are in phase alongside the out-of-plane x-axis. Since the excitation beams superimpose on the sample and induce a modulation of the electric field along the in-plane z-axis, a macroscopic electromagnetic wave propagates through the ionic lattice in the in-plane direction. The coupling between a transverse optical phonon mode and an induced electric field of comparable frequency and wave vector is defined as phonon-polariton. The strong coupling between light and phonons is shown in the dispersion relation in fig.1.2. In the long wavelength range the phonon-polaritons branch approaches the electromagnetic light graph in the ionic material, which is indicated as c/n_{THz}. The refractive index of the sample in the terahertz region is n_{THz}.
To excite phonon-polaritons, the sample that is excited needs to host infrared and Raman active phonon modes that occur in a non-centrosymmetric unit cell [15]. In addition, to avoid high absorption of the electromagnetic waves incident on the sample, the probed materials are transparent. Ferroelectric materials satisfy these properties, resulting in their broad usage for the study of phonon-polaritons [16]. In polaritonics lithium niobate ($LiNbO_3$) and lithium tantalate ($LiTaO_3$) are frequently used due to their low phonon damping rate and high refractive indices in the terahertz range combined with large non-linear optical coefficients [17].

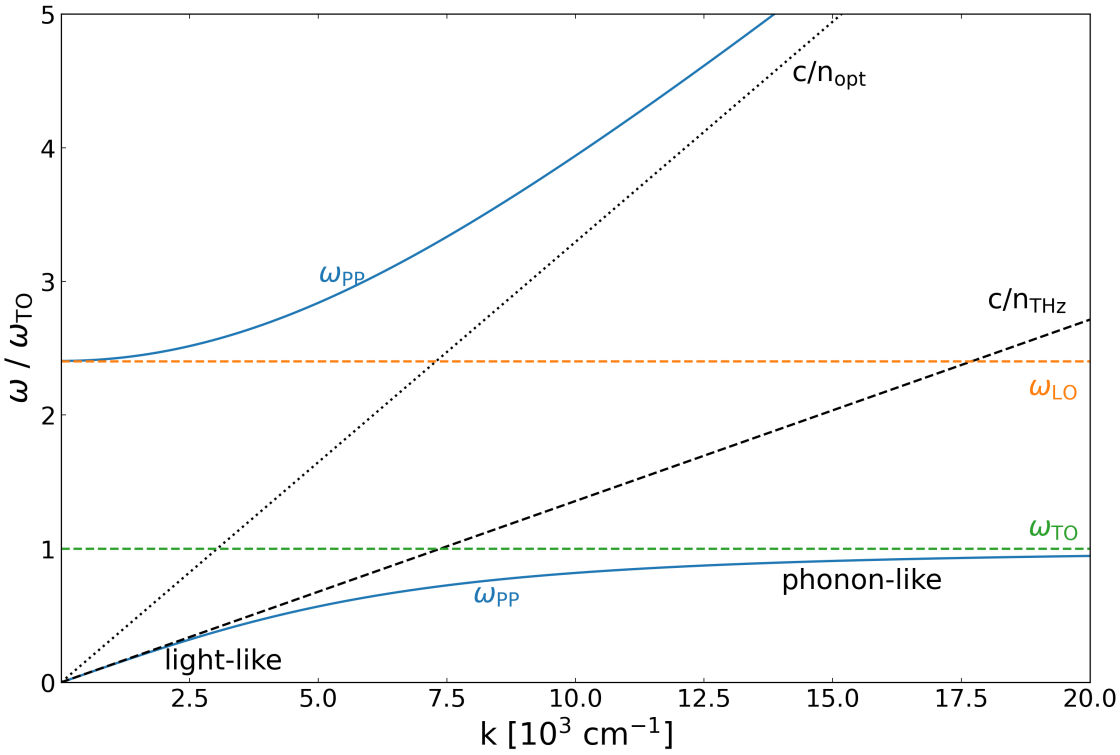

Figure 1.2.: Calculated dispersion relation for phonon-polaritons in ionic materials with refractive index n with arbitrary chosen parameters in blue. Additionally, the transverse optical phonon with eigenfrequency ω_{TO} represented as dashed green line and longitudinal optical phonon indicated as dashed orange line are depicted. In between, the region of perfect reflection is located. In the short and long wavelength-range, the graph of the polaritons approach the photon dispersion. The refractive indices $n_{THz} = 6.8$ and $n_{opt} = 2.18$ correspond to the refractive indices in the terahertz and optical frequency, thus low and high wavelength region of the probed sample.

1.2. Selective excitation of phonon-polaritons in $LiNbO_3$

This section discusses the general concept of a wave vector selective generation of phonon-polaritons in $LiNbO_3$. The pulse duration of the excitation laser is on the order of 150 fs, which is significantly shorter than the period of the excited lattice modes that are on the order of 500 fs. Thus, the light acts an impulsive force for the generation of phonon-polaritons. This has been described extensively, for example in the PhD thesis of Brennan [18]. Here, I provide a short schematic overview.
Before propagating through the sample, the femtoseconds laser pulses are separated into two coherent laser pulses, as described in section 2.1. They intersect in air at an angle Θ_{air}, shown in fig.1.1. This type of excitation and detection is a four-wave mixture applied in a transient grating setup, since another femtosecond pulse, the probe pulse diffracts partially at the excited material, and is incident at the detector. This impulsive stimulated scattering (ISS) is schematically shown in fig.1.3. The impulsive force on the phonons is an impulsive stimulated Raman scattering (ISRS) mechanism [19]. The interfering electric fields of the excitation pulses induce a transient grating of the electric field resulting in a spatially modulated oscillation amplitude of the atoms, which wavelength is depending on the intersection angle in air Θ_{air}. A maximum in the intensity of the electric field corresponds to a large oscillation amplitude of the atom. The oscillating atoms in turn result in a modulated refractive index from which the probe pulse is diffracted.

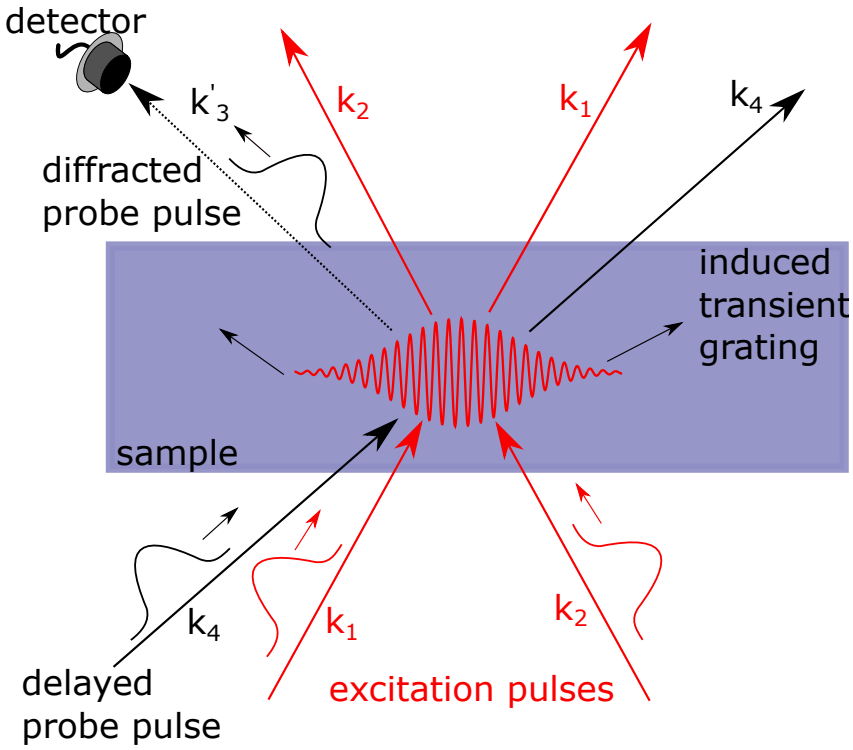

Figure 1.3.: Configuration of the ISS process, the four-wave mixture in the transient grating setup explains excitation and detection of the signal consisting of the diffracted light of the delayed probe pulse.

1.2.1. Impulsive stimulated Raman scattering

As described in fig.1.3, I consider two excitation pulses with wave vector $\mathbf{k}_1$ and $\mathbf{k}_2$ intersecting at the sample with the angle Θ, which is related to the intersection angle in air Θ_{air} via Snell's law of refraction. Due to the experimental setup, furthermore explained in chapter 2, the excitation spot is elliptically shaped. This is shown in fig.1.4. Since both excitation pulses are invested with the same spectrum, fig.1.5 considers two cases, $|\mathbf{k}_1| > |\mathbf{k}_2|$ and $|\mathbf{k}_1| < |\mathbf{k}_2|$.

ISRS processes are governed by energy and momentum conservation, described in the following. E_1 and E_2 are photon energies of the excitation pulses, and $E_{PP} = \hbar\omega_{PP}$ is the energy of the generated phonon-polariton. This yields:

$$E_{PP} = |E_1 - E_2|$$

which is schematically shown in fig.1.5a). Since the stimulating pulse has a larger energy magnitude compared to the pump pulse, this process is described by Stokes scattering. I discuss the case $|\mathbf{k}_1| > |\mathbf{k}_2|$, $E_1 > E_2$ in the following. The beam with energy E_1 excites the ground state of the crystal G to the excited virtual state V. The laser used in this experiment has a finite spectral width, as elaborated in section 2.1 resulting in the smeared excitation energy range around V and E. The difference between the energy states E and G defines the energy of the phonon-polariton. The momentum conservation describes the partition of $\mathbf{k}_1$ into $\mathbf{k}_2$ and $\mathbf{k}_{PP}$, which in the considered case indicates a left propagating phonon-polariton. For the case $|\mathbf{k}_1| < |\mathbf{k}_2|$ the arguments apply vice versa, a right propagating phonon-polariton arises.

For the probe process, the energy and momentum conservation is schematically shown in fig.1.6. In accordance to the detection process displayed in fig.1.4 where the probe pulse corresponding to $\mathbf{k}_3$ is blocked. The wave vector $\mathbf{k}_4$ is shifted by left or right propagating phonon-polaritons into the same direction the blocked probe pulse would have propagated. In that case, the signal is

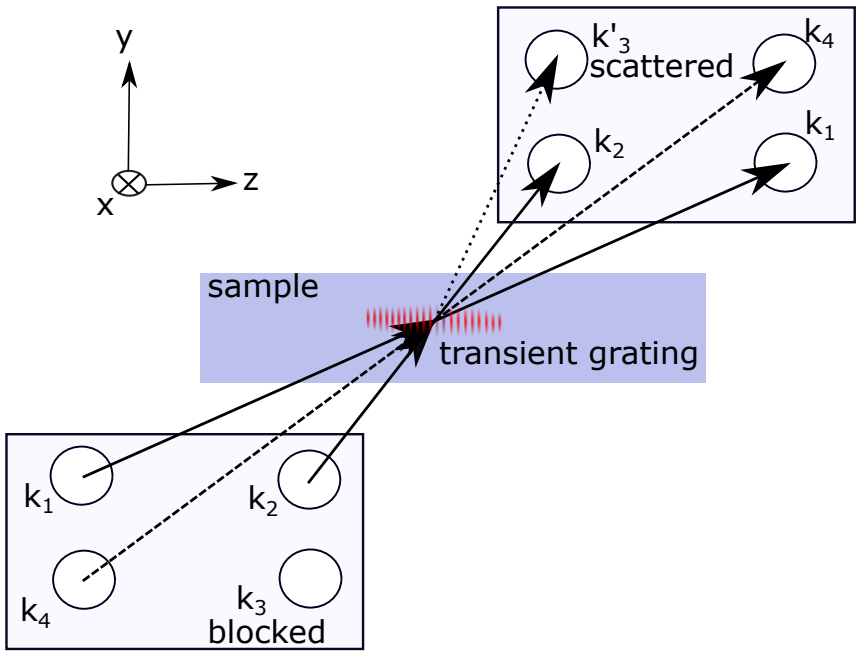

Figure 1.4.: Sketch of box-CARS geometry, used in the following four-wave mixing experiments; $\mathbf{k}_1$ and $\mathbf{k}_2$ interfere at the position of the transparent sample to produce a transient grating, where the $\mathbf{k}_4$-vector is diffracted to the direction of $\mathbf{k}_3'$ by ISRS. The wave vectors $\mathbf{k}_1$ and $\mathbf{k}_2$ lie within the x-z-plane.

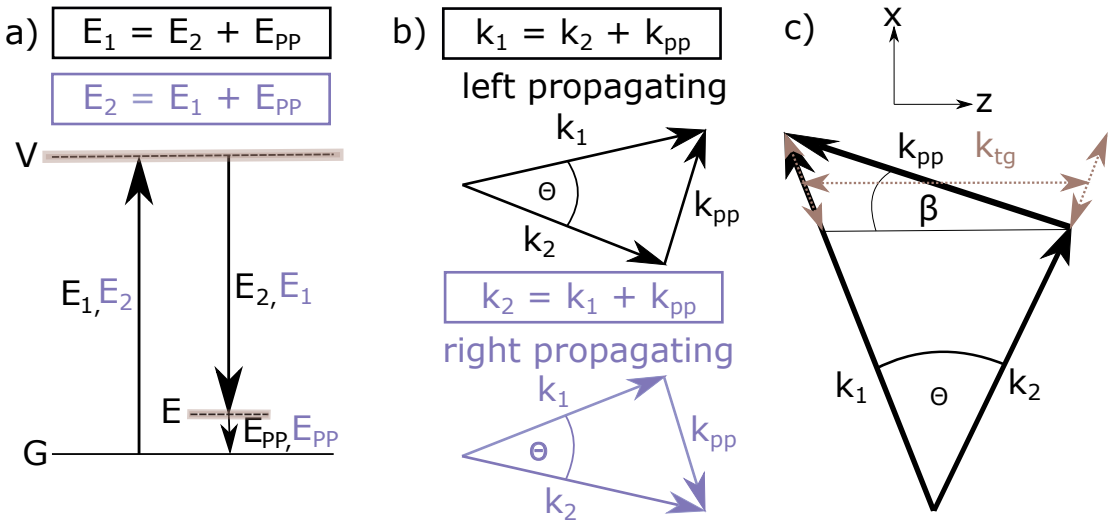

Figure 1.5.: Schematic visualization of the generation process of phonon-polaritons via Stokes scattering. It requires energy conservation, depicted in a) and momentum conservation, depicted in b). In c) a comparison between the direction of the wave vector of the modulation of the electric field $\mathbf{k}_{tg}$ at the sample (i.e. transient grating) and the phonon-polariton wave vector is shown. Apparent values for $\mathbf{k}_1$ and $\mathbf{k}_2$ due to the spectral width of the laser pulses are implied in beige. Left and right are defined from the top view, like in fig.1.1b) from which the system of coordinates is adapted.

detected along the $\mathbf{k}_3$-direction as implied in fig.1.3. In contrast to the pump process, Stokes and anti-Stokes scattering occurs, the phonon-polaritons act as seed in the anti-Stokes process. The Stokes process describes the stimulated generation of left propagating phonon-polariton, where an already existing left propagating phonon-polariton acts as seed. The incident beam with wave vector $\mathbf{k}_4$ decomposes into a left propagating phonon-polariton and a wave vector in the $\mathbf{k}_3$-direction. In contrast, the anti-Stokes process corresponds to the annihilation of right propagating phonon-polaritons as indicated in fig.1.6b). In the following analysis, I approximate that the Stokes and Anti-Stokes process are equally likely, and therefore the spectrometer detects both of them. Since

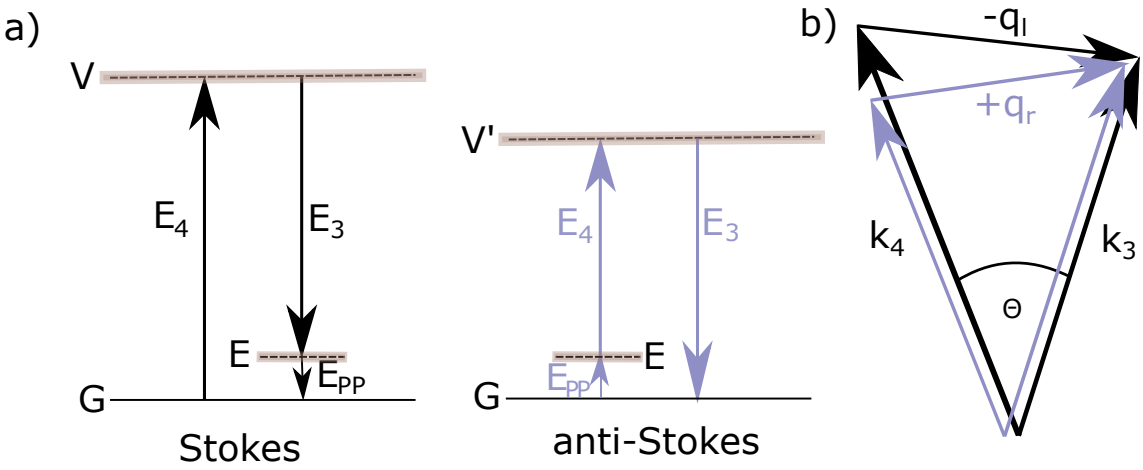

Figure 1.6.: Sketch of detection of the phonon-polaritons via Stokes and anti-Stokes scattering that again fulfill energy and momentum conservation, depicted in a) and b). In the Stokes process, the incident beam experiences a red shift, for the anti-Stokes a blue shift with respect to the energy of the incident beam.

left and right propagating phonon-polaritons contribute to the signal detected in the spectrometer on a specific pixel dedicated to the energy $\hbar\omega_3$, not solely the actual frequency but also another analyzed frequency that equals twice the actual frequency of the phonon-polariton with wave vector q may occur. To prevent this effect additional notch filters may be mounted in the setup, as discussed by Crimmins et al. [20], which results in a more well-defined wave vector to e.g. avoid right propagating phonon-polariton by decreasing the average wave vector of $\mathbf{k}_1$ [21, chapter 7]. However, a reduction of the spectrum also reduces the time-resolution, which may render the excitation of high-frequency phonon-polaritons inefficient. The spectrometer is located along the $\mathbf{k}_3$-direction

According to the Boltzmann distribution, all observed phonon-polariton modes $< 6\,\mathrm{THz}$ * are occupied at room temperature T=300K. However, the amount of thermally excited phonon-polaritons is negligibly small compared to the amount of phonon-polaritons excited by ISRS [22], [23].

1.2.2. Propagation direction of phonon-polaritons

As depicted in fig.1.5c) the propagation direction of the phonon-polariton k_{PP} is slightly different to the wave vector of the transient grating which is collinear to the sample surface, because the energy distribution of the excitation pulses results in a smeared momentum distribution. Every set of scattered wave vectors that obey energy and momentum conservation contribute to the generation of phonon-polaritons. The wave vector $\mathbf{k}_{tg}$ corresponds to the average over the beige excitation region in fig.1.5c). By trigonometry the magnitude of the wave vector of the transient grating k_{tg}

*Calculated from the average thermal energy at room temperature of k_BT=25 meV.

can be calculated [†] from the magnitude of the central excitation wave vector k_{exc}

$$k_{tg} = 2k_{exc} \cdot \sin\frac{\Theta}{2}. \tag{1.1}$$

Proceeding from this the wave vector of the phonon-polariton can be determined. Considering the coordinates from fig.1.5c), the wave vector of the phonon-polaritons, $\mathbf{k}_{PP}$, in the following called q, consists of two non-zero components derived by trigonometrical relations:

$$q_x = |k_1 \cos\frac{\Theta}{2} - k_2 \cos\frac{\Theta}{2}| = \cos\frac{\Theta}{2} \cdot (|k_1 - k_2|) \tag{1.2}$$

$$q_z = |k_1 \sin\frac{\Theta}{2} + k_2 \sin\frac{\Theta}{2}| = \sin\frac{\Theta}{2} \cdot (|k_1 + k_2|). \tag{1.3}$$

Since the excitation pulses are governed by the Gaussian distribution, the central excitation wave vector yields $\mathbf{k}_{exc} = (\mathbf{k}_1 + \mathbf{k}_2)/2$, by applying the momentum conservation

$$\mathbf{k}_{1,2} = \mathbf{k}_{exc} \pm \mathbf{q}/2.$$

the z-direction of the wave vector in equation 1.3 can be re-written from equation 1.1

$$q_z = \cos\frac{\Theta}{2} \cdot 2k_{exc}$$

$$q_z \approx k_{tg}. \tag{1.4}$$

Additionally the x-direction combined with the energy conservation $\omega_{PP} = c_{opt}(|k_1 - k_2|)$ can be determined, yields to the total q vector of the phonon-polariton

$$q^2 = q_x^2 + q_z^2 = \left(\frac{\omega_{PP}}{c_{opt}}\right)^2 \cos^2\frac{\Theta}{2} + k_{tg}^2 \tag{1.5}$$

Whereby c_{opt} is the velocity of an electromagnetic wave in the sample at optical frequency range. The direction of propagation is described by trigonometrical calculation derived from fig.1.5c)

$$\cos\beta = \frac{k_{tg}}{q} \tag{1.6}$$

Both $\mathbf{q}$ and $\mathbf{k}_{tg}$ depend on Θ, which is adjusted by the setup. See section 2.1.
The intersection angle in air Θ_{air} is derived in appendix B. Using the components of the optical setup yields

$$\Theta_{air} = 2\arctan\left(\frac{f_1\lambda_{exc}}{f_2\lambda_{PM}}\right). \tag{1.7}$$

With the focal lengths of the cylindrical lens and spherical lens (cf. fig.2.2) f_1 and f_2, the central wavelength of the excitation pulse λ_{exc} and the wavelength of a phase mask pattern λ_{PM} which is also adjusted by the setup (cf. section 2.1).
By taking Snell's law of refraction into account, the intersection angle at the sample can be calculated with the refraction index of the sample at optical frequencies n_{opt}, mentioned in the next section. The small-angle approximation is applied since Θ_{air} is smaller than 10° (cf. eq.B.8).

$$\Theta = \frac{n_{air}}{n_{opt}}\Theta_{air}$$

[†] For this thesis the wavelength of the transient grating determined by measurement

1.3. Crystal structure and optical properties of $LiNbO_3$

Lithium niobate, respectively $LiNbO_3$, is a birefringent ferroelectric material, which is transparent because of its band gap that is on the order of 4 eV. The optical axis corresponds to the c-axis of the crystal. The polarization of the electric field of the beam is set parallel to the c-axis. Since the phonon-polaritons propagate mainly in that direction, their electric field is orientated perpendicular to the c-axis, thus transverse optical phonon modes are excited. Thus, the ordinary refractive index is considered. The ferroelectric polarization occurs also along this crystal axis. The Li^+ and Nb^{5+} atoms within the unit cell break the symmetry of the crystal along the c-axis. One of the transverse optical phonon modes is shown in fig.1.7, i.e. the motion of lithium and niobate along the c-axis. In order to excite phonon-polaritons with a high efficiency and facilitate the measurement, the electric field of the incident beams is polarized parallel to the optical axis, i.e. the c-axis of the ferroelectric sample.
The extraordinary refractive index is n_e=2.18 for 800 nm, which is in this thesis also called n_{opt} [24, page 9], [25]. In this thesis, only $LiNbO_3$ fabricated in so called x-cut, shown in fig.1.7b) is discussed. In that material, the c-axis lies within the plane of the sample surface [26]. In this work, I chose the polarization of the incident beams to be parallel to the c-axis if not stated otherwise, e.g. the sample rotation series discussed in section 3.2. Relevant properties of lithium niobate are listed in table 1.1

Table 1.1.: Relevant properties of lithium niobate at room temperature and standard pressure [27],[28]. Since the refractive index is frequency-dependent, the value for the optical range is taken at 800 nm (375 THz) [29], respectively the value for the terahertz range at 1 THz [30].

property	formula symbol	value
density	ρ	4.65 g/cm^3
band gap	E_g	3.7 eV
refractive index (optical range), ordinary	$n_{opt,o}$	2.26
refractive index (optical range), extraordinary	$n_{opt,eo}$	2.18
refractive index (terahertz range), ordinary	$n_{THz,o}$	6.8
refractive index (terahertz range), extraordinary	$n_{THz,eo}$	4.91

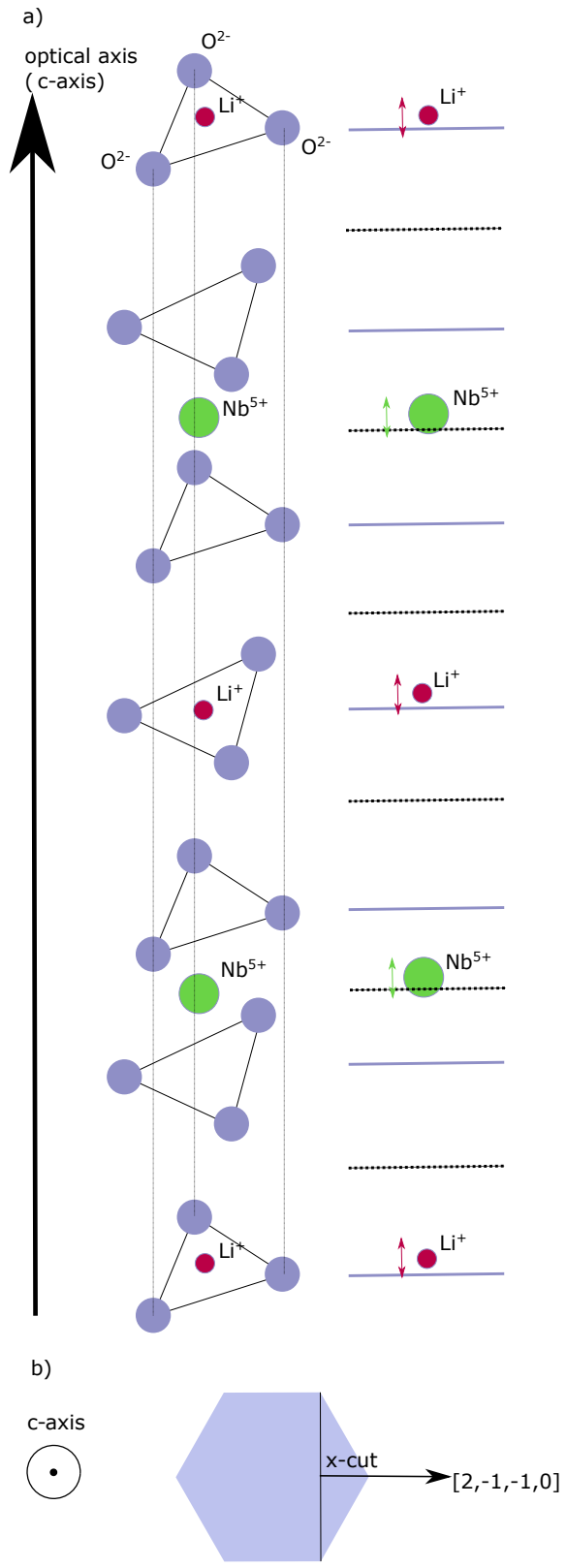

Figure 1.7: Schematic depiction of the crystal structure of $LiNbO_3$. View along the c-axis a): This depiction shows two unit cells on top of each other along the c-axis. The oxygen atoms in blue are arranged in two distorted plains of each three atoms perpendicular to the optical axis, resulting in a hexagonal configuration. The lithium atoms in red are located above the planes. The niobium atoms are slightly above the center of two oxygen triangles. The hexagon in b) represents the view down the c-axis and indicates the direction of the x-cut. This figure is adapted from [21, page 7]

1.4. Phonon-polariton dispersion relation in bulk $LiNbO_3$

The next two sections contain the theoretical background which is required to derive the dispersion relation within two specimens with different out-of-plane thickness. I consider one bulk specimen of 1 mm thickness and a waveguide of 50μm thickness consisting of $LiNbO_3$. I will approach the dispersion relation of the bulk by considering the Lorentz oscillator model, from which the permittivity and therefore the refractive index are deduced. The additional quantization due to the boundary condition of the thin slab waveguide is central to the excitation and propagation of phonon-polaritons modes in a $LiNbO_3$ waveguide.
The Lorentz oscillator model assumes that an electric field E(t) excites the motion of electrons in particular and charged particles in general. The electron with mass m bounded to the atomic core can be approximated using a driven harmonic oscillator [31] as depicted in fig.1.8. The following derivation is based on lecture 39 by Colton [32]. The equation of motion yields with damping Γ, resonance frequency ω_0, mass of electrons m with charge q:

$$m\frac{\mathrm{d}^2x}{\mathrm{d}t^2}+m\Gamma\frac{\mathrm{d}x}{\mathrm{d}t}+m\omega_0^2x=-qE(t) \tag{1.8}$$

The solution of the driven harmonic oscillator equation 1.8 is the Lorentzian function:

$$x(\omega,t)=-\frac{q}{m}\frac{1}{\omega_0^2-\omega^2-i\Gamma\omega}E(t). \tag{1.9}$$

The observable real space displacement is given by the real part of equation 1.9. The electric dipole moment p_{elec} can be re-written in two different ways, that are used to identify the polarizability $\alpha(\omega)$ as:

$$\begin{aligned} -q\cdot x(\omega,t)&=p_{\mathrm{elec}}=\varepsilon_0\alpha(\omega)E(t)\\ \Rightarrow\alpha(\omega)&=\frac{-qx(\omega,t)}{E(t)}=\frac{q^2}{m\varepsilon_0}\frac{1}{\omega_0^2-\omega^2-i\Gamma\omega}. \end{aligned} \tag{1.10}$$

Now two expressions for the polarization P of N independent oscillating atoms in a specific volume V yield P=$\chi(\omega)$ E(t) and P=$\frac{N}{V}\alpha(\omega)$ E(t) resulting in a relation between the susceptibility $\chi(\omega)$ and polarizability $\alpha(\omega)$ from which the dielectric function can be derived:

$$\begin{aligned} \chi(\omega)&=\frac{N}{V}\alpha(\omega)\\ \varepsilon(\omega)&=1+\chi(\omega)=1+\frac{N}{V}\alpha(\omega)\\ \varepsilon(\omega)&=1+\frac{Nq^2}{Vm\varepsilon_0}\frac{1}{\omega_0^2-\omega^2-i\Gamma\omega}. \end{aligned}$$

By considering the five significant transverse optical modes, which I provide with the index i and define n_V=N/V

$$\varepsilon(\omega)=1+\sum_{i=1}^{5}\frac{n_{V,i}q^2}{m\varepsilon_0}\frac{1}{\omega_{0,i}^2-\omega^2-i\Gamma\omega}. \tag{1.11}$$

In a dielectric solid like $LiNbO_3$, there exist more than one type of polar vibration modes. Hence, resonances in the range of ultraviolet or infrared light, e.g. atomic electron transition of valence (ultraviolet) or near-core electrons (infrared) resulting in a higher dielectric limit for $\omega\gg\omega_0$, which was up to now assumed to be 1 and now set to ε_∞. The higher dielectric limit for $\omega\to\infty$ remains to

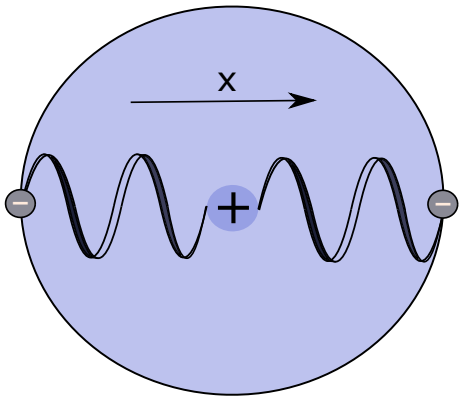

Figure 1.8.: Sketch of the bonding between two electrons and the atomic core, the bonding is approximated with the Lorentz oscillator model

be 1.
Deriving the dielectric function quantum-mechanically, as described in [14], I obtain

$$\varepsilon(\omega) = \varepsilon_\infty + \sum_{i=1}^{5} \frac{\omega_{0,i}^2(\varepsilon_{0,i} - \varepsilon_\infty)}{\omega_{0,i}^2 - \omega^2 - i\Gamma_i\omega}. \tag{1.12}$$

Thus, by comparing equation 1.11 and equation 1.12 two adjustments become evident: As mentioned above, the limit of dielectric function for high frequencies modifies from 1 to $\varepsilon_\infty = 5.0$, which is material-specific. Every material-dependent value, $\omega_{0,i}, \Gamma_i, \varepsilon_{0,i}$ and ε_∞, in the following, has been measured by Barker and Loudon [33] via Raman scattering spectroscopy. There also the five relevant transverse-optical modes are depicted.
Secondly, $n_{V,i}$ can be extracted by comparison of equation 1.11 and equation 1.12:

$$n_{V,i} = \frac{(\varepsilon_{0,i} - \varepsilon_\infty)\omega_{0,i}^2 m\varepsilon_0}{q^2} \tag{1.13}$$

In that picture, the independent oscillating atoms per volume $n_{V,i}$ may be interpreted as a modified oscillator strength of mode i, which is generally identified as $\varepsilon_{0,i}$-ε_∞. Since the unit of the particle density is $[n_{V,i}]=\frac{1}{m^3}$, it describes the quantity of atoms oscillating with a specific resonance frequency $\omega_{0,i}$ for a particular mode i. The resulting dielectric function of the modified equation 1.11 is visualized in fig.1.9 using the parameters given in table 1.2.

Table 1.2.: Data of Raman spectroscopy of $LiNbO_3$, computing equation 1.13 yields $n_{V,i}$ which has not been reported by Barker and Loudon [33] by room temperature experiments

mode i	$\omega_{0,i}/2\pi$ in cm^{-1}	$\Gamma/2\pi$ in cm^{-1}	$\varepsilon_{0,i}$-ε_∞	$n_{V,i}$ in $\cdot 10^{23}\frac{1}{m^3}$
1	152	14	22	56.7
2	265	12	5.5	43.1
3	322	11	2.2	25.4
4	363	10	2.3	33.7
5	586	35	3.3	126.4

The frequency of the phonon-polaritons can be calculated from the following relation:

$$\omega_{PP} = c \cdot k = \frac{c_0}{n(\omega)} \cdot k = \frac{c_0}{\sqrt{\varepsilon(\omega)}} \cdot k,$$

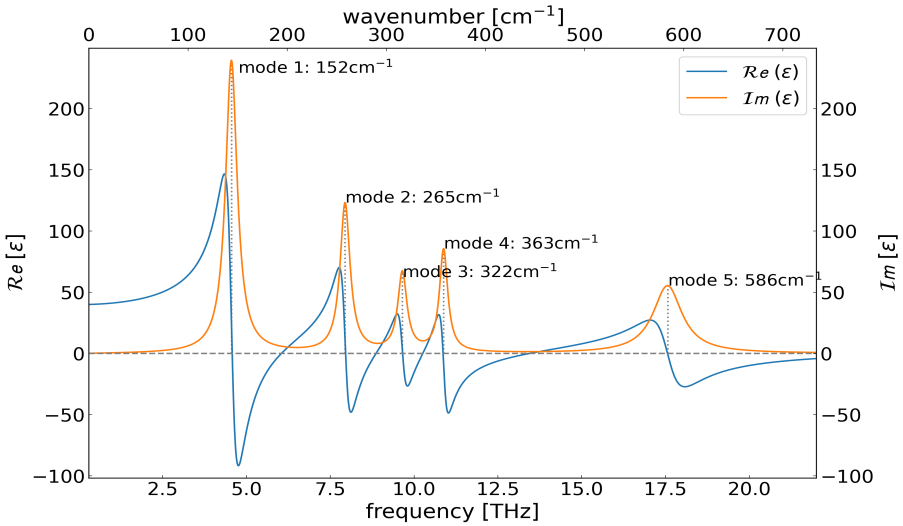

Figure 1.9.: Graph of the resulting real and imaginary part of the dielectric function of bulk $LiNbO_3$ for electric fields polarized along the ordinary direction with annotated resonance frequencies

and the resulting dispersion relation $\omega(k)$ is given in fig.1.10. The dispersion relation applies for bulk $LiNbO_3$ where the incoming light is polarized along the c-axis. In a), the frequency-dependent damping proportionality to the dispersion relation graph is depicted and the magnitude of the blue line increases in the vicinity of the five phonon resonances depicted as dotted lines. On the other hand side in b) the blue graph approaches the black line representing the coupling to light in the terahertz region as mentioned in fig.1.2

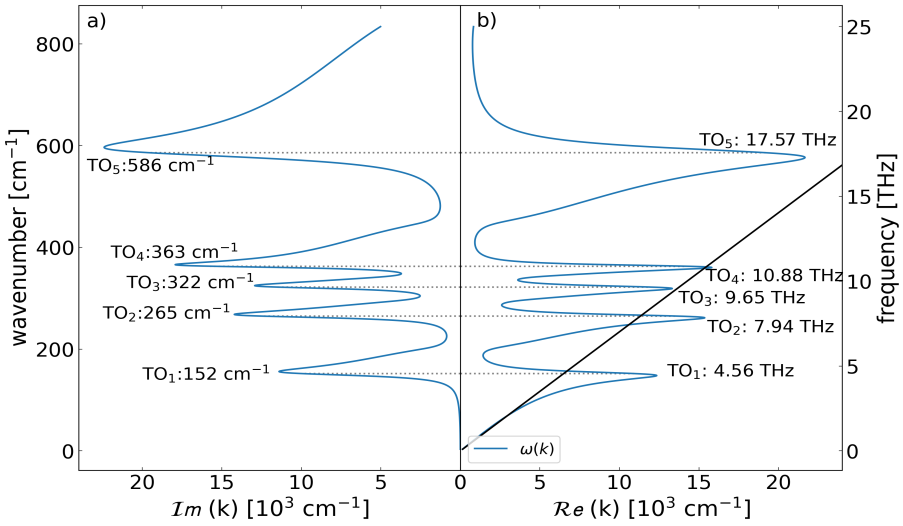

Figure 1.10.: Computed dispersion relation of phonon-polaritons in $LiNbO_3$. The calculation for the imaginary part of the wave vector in a) and the real part of the wave vector in b) used the parameters from reference [33]. The dotted lines represent the four transverse optical modes in $LiNbO_3$. The black curve in b) shows the dispersion relation of light that experiences a constant average ordinary refractive index in the terahertz range $n_{THz} \approx 6.8$ [30].

1.5. Phonon-polariton dispersion relation in a waveguide

To understand the dispersion in waveguides of $LiNbO_3$ I consider a planar dielectric waveguide which is excited by wavelengths comparable to the thickness of the waveguide itself. In contrast to the bulk, a thin specimen exhibits a quantization condition resulting in only certain discrete angles Θ_i that allow propagating phonon-polaritons inside the waveguide. This leads to the fact that several waveguide modes are possible, for a given wave vector. The wave vector of the phonon-polariton yields k_0. An extensive derivation is presented in [34]. In the following derivation, I examine first an infinite plane boundary between two dielectrics with refractive index n_1 and n_2, where $n_2 < n_1$, which is shown in fig.1.11. In the following the angle Θ_i describes the propagation angle of infrared light, respectively phonon-polaritons, similar to β corresponding to the bulk, derived in section 1.2.2. One boundary condition for this problem is that the in-plane part of the k-vectors are equal

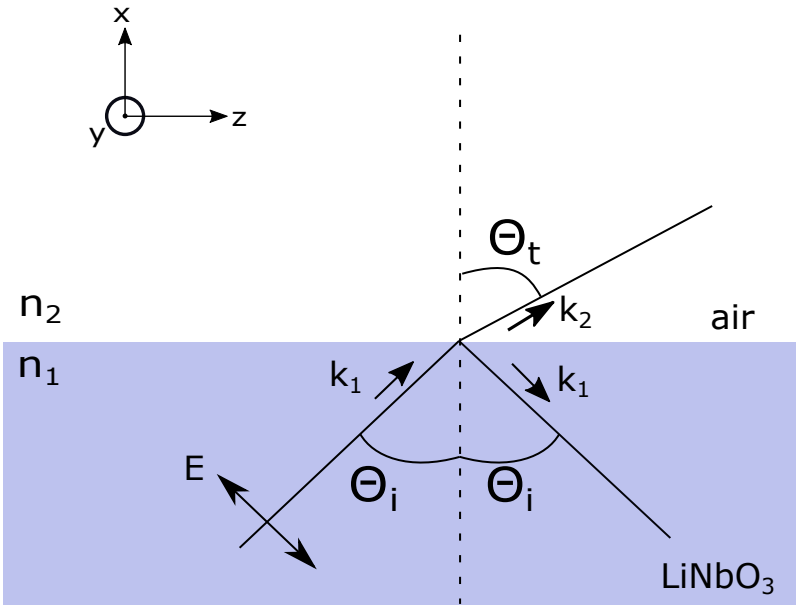

Figure 1.11.: Reflection and transmission at a dielectric boundary, where $n_2 < n_1$

for the incident (i), reflected (r) and transmitted (t) beam.

$$k_{1z} = k_{2z} \tag{1.14}$$

with use of equation 1.14 and trigonometry, e.g. $k_{1x} = k_0 n_1 \cos\Theta_i$, $k_0 = \omega/c$ the Fresnel equations arise as a result with the assigned index P for the case of p-polarized light that is used in our setup.

$$\begin{aligned} R_P &= \left(\frac{E_{0r}}{E_{0i}}\right)_P = \frac{k_{1x}n_2^2 - k_{2x}n_2^2}{k_{1x}n_2^2 + k_{2x}n_1^2} \\ T_P &= \left(\frac{E_{0t}}{E_{0i}}\right)_P = \frac{2k_{1x}n_1n_2}{k_{1x}n_2^2 + k_{2x}n_1^2} \end{aligned} \tag{1.15}$$

Applying trigonometry in fig. 1.11 yields

$$\begin{aligned} k_{2x}^2 &= n_2^2k_0^2 - k_z^2 \\ \Rightarrow k_{2x}^2 &= (n_2^2 - n_1^2\sin^2\Theta_i)k_0^2 \end{aligned} \tag{1.16}$$

Hence, k_{2x} is imaginary for the condition $\sin\Theta_i > n_2/n_1$, and I define $k_{2x} = -i\cdot\gamma$. Applying this to equation 1.15 we then obtain:

$$\left(\frac{E_{0r}}{E_{0i}}\right)_P = \frac{k_{1x}n_2^2 + i\cdot\gamma n_1^2}{k_{1x}n_2^2 - i\cdot\gamma n_1^2} = e^{i2\Phi} \tag{1.17}$$

where the phase equals

$$\Phi = \arctan\left(\frac{\gamma n_1^2}{k_{1x}n_2^2}\right) \tag{1.18}$$

Using the definition for k_{2x}, substituting 1.16 and using the trigonometrical expression for k_{1x} yields

$$\Phi = \arctan\left(\frac{n_1^2}{n_2^2}\sqrt{\frac{n_1^2\sin^2\Theta_i - n_2^2}{n_1^2\cos^2\Theta_i}}\right) \tag{1.19}$$

Since the magnitude of the reflectivity R in equation 1.17 equals 1 in all cases, it describes the phenomenon of total internal reflection, i.e. the reflected wave is unchanged in its amplitude compared to the incident wave but experiences a phase change. The condition mentioned above, $\sin\Theta_i > n_2/n_1$ ensues from Snell's law of reflection by setting $\Theta_t = \pi/2$, such that total internal reflection occurs. Since the absolute value of $\sin\Theta_i$ is limited by 1, n_1 is larger than n_2. In the following I assume n_2=1 and medium 1 n_1=6.8 which correspond to the refractive index of air and $LiNbO_3$ respectively are set for the calculations and graphs to follow. The phonon-polaritons propagate along the extraordinary axis as mentioned in section 1.3 so that their electric field component is perpendicular and experiences the ordinary refractive index [6]. The following section covers the case where the beam propagates inside the waveguide undiminished due to perfect total internal reflection and lossless propagation. The propagation of phonon-polaritons is illustrated in fig.1.12. Please note the additional dielectric interface parallel to the first one at a distance 2d. Considering total internal reflection we can express the electromagnetic wave in air by

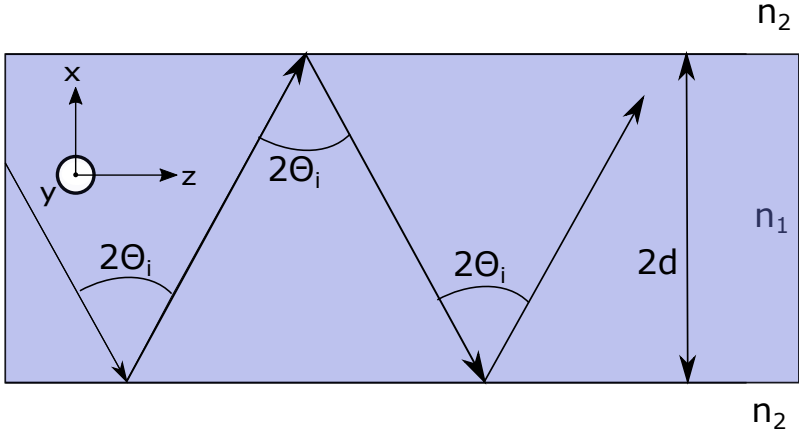

Figure 1.12.: Propagation of an electromagnetic wave in a dielectric slab-waveguide

substituting **k** = (k_{2x},0,k_z) and the definition for k_{2_x}:

$$\begin{aligned} E &= E_0 e^{i(\omega t - \mathbf{kr})} \\ &= E_0 e^{-\gamma x} e^{i(\omega t - k_z z)} \end{aligned} \tag{1.20}$$

This indicates an evanescent wave, resulting in an electric field outside the sample. I will distinguish between E_{core} inside the waveguide and $E_{cladding}$ describing the electric field in medium 2, both are derived in the end of this chapter.

The eigenvalue equation

The waveguide geometry imposes boundary conditions on the electromagnetic wave, which result in quantized modes. To obtain an adequate expression for the phase, I concentrate on the x-direction of the k-vector inside the waveguide. In fig.1.13 two waves are depicted which are genuinely similar because they are a reflection of themselves. They interfere constructively, if the overall phase change α imposed by the wave of twofold crossing and reflecting inside the waveguide is a multiple of 2π. We can find the phase change upon reflection:

$$\begin{aligned} 2m\pi &= \underbrace{2 \cdot k_{1x} 2d - 2 \cdot \Phi}_{\alpha} \\ \Rightarrow \Phi &= k_{1x} d - \frac{m\pi}{2} \end{aligned} \tag{1.21}$$

By comparing equation 1.19 with equation 1.21 I can re-write:

$$\begin{aligned} &\tan\left(k_{1x} d - \frac{m\pi}{2}\right) = \frac{n_1^2}{n_2^2} \sqrt{\frac{n_1^2 \sin^2\Theta_i - n_2^2}{n_1^2 \cos^2\Theta_i}} \\ \Leftrightarrow &\underbrace{\tan\left(k_0 n_1 \cos\Theta_i d - \frac{m\pi}{2}\right)}_{F1} = \underbrace{\frac{n_1^2}{n_2^2} \sqrt{\frac{n_1^2 - n_2^2 - n_1^2 \cos^2\Theta_i}{n_1^2 \cos^2\Theta_i}}}_{F2}, \end{aligned} \tag{1.22}$$

which is called the eigenvalue equation for transverse magnetic modes (TM), that occur when the electric field is polarized parallel to the plane of incidence (p-polarized). By applying non-negative integers for n different modes are selected, i.e. m = 0,1,2,... enumerates the orders of the transverse magnetic modes. In fact, if I consider s-polarized light, transverse electric modes (TE) arise. Equation 1.22 is a transcendent equation. A common approach to solve it, is to plot the

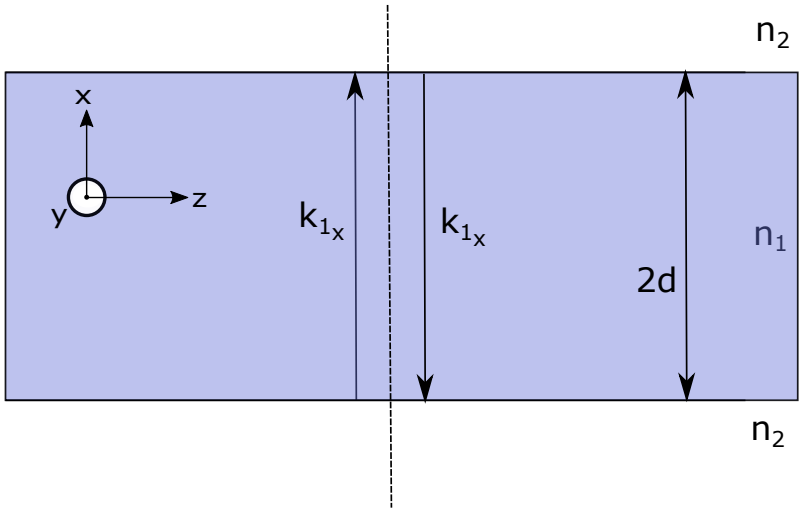

Figure 1.13.: Wave vectors of two waves inside the waveguide, visualizing the boundary conditions for quantized waveguide modes. X=0 defines the center of the waveguide.

left- and right-hand side of 1.22 for different m as shown in fig.1.14. By identifying the graphical intersections of F1 with F2, I obtain the angle of propagation Θ_i and the corresponding k_{1x}-vector and γ for each mode as listed in tab.1.3.

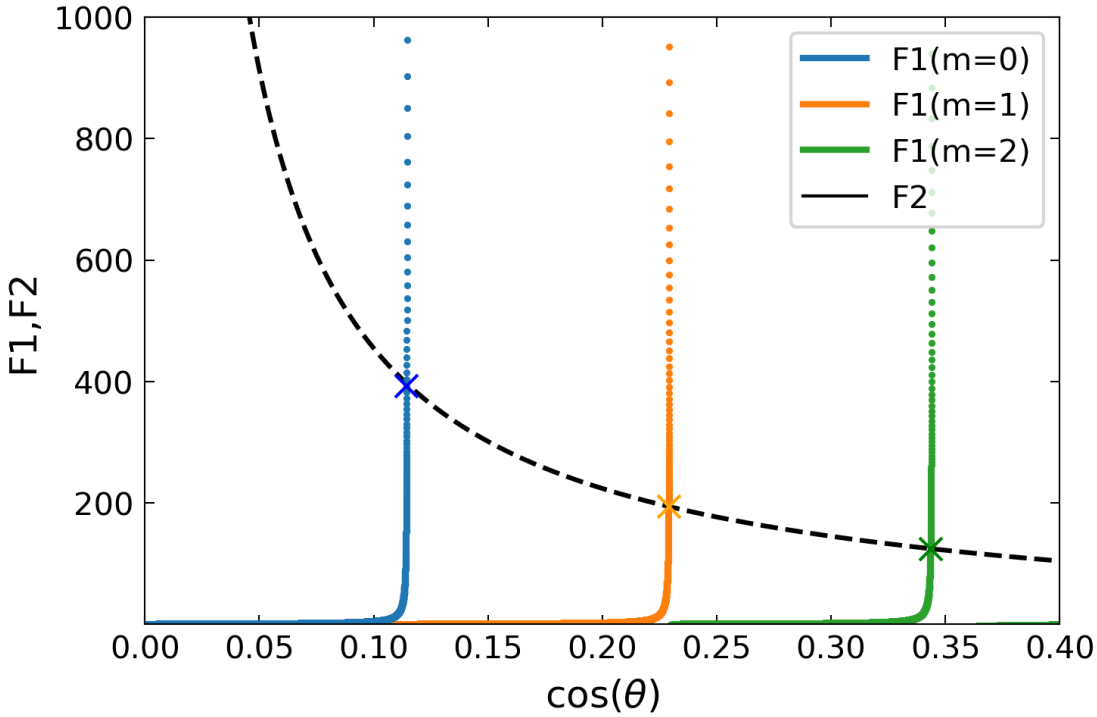

Figure 1.14.: Graphical solution of the eigenvalue equation including the first three transverse magnetic (TM) modes, F1 and F2 on the y-axis as defined in equation 1.22.

Electric field pattern

As mentioned above, in fig.1.1 the terahertz electric field of the phonon-polaritons inside the thin slab points in the in-plane y-direction. From fig.1.13 the direction of propagation is set to x-direction, i.e.

$$\begin{aligned} E_y(x) &= E_y(x)^+ + E_y(x)^- \\ &= E_0 \cdot e^{-ik_{1x}x} + E_0 \cdot e^{+i(k_{1x}x+\Gamma)} \\ \Rightarrow E_y(0)^+ &= E_0 \text{ and } E_y(0)^- = E_0 e^{i\Gamma} \end{aligned} \tag{1.23}$$

where Φ is a phase angle determined by the total phase change of the electric wave that traverses the waveguide twice. The phase change for the propagating wave from the center (x=0) to the boundary, reflecting and return is πn. As a result, re-writing and arranging equation 1.23 yields

$$\begin{aligned} E_y &= \underbrace{E_0 e^{-i\frac{m\pi}{2}}}_{\frac{1}{2}E_0'} \left(e^{-i(k_{1x}x-\frac{m\pi}{2})} + e^{+i(k_{1x}x-\frac{m\pi}{2})} \right) \\ &= E_0' \cos(k_{1x} - \frac{m\pi}{2}). \end{aligned} \tag{1.24}$$

The electric field beyond the boundaries of the waveguide is given by

$$E_y = \begin{cases} Ae^{-\gamma x} & \text{, for } x > d \\ Ae^{\gamma x} & \text{, for } x < -d \end{cases}, \tag{1.25}$$

wherein A represents the magnitude of the electric field at the boundary, that must satisfy the condition of continuity across the interface. The values in tab.1.3 are used to determine the electric field in fig.1.16.

Table 1.3.: Characteristics of the first three TM modes (m=0,1,2) within a 50μm thick $LiNbO_3$ waveguide, which result from the numerical solution of the eigenvalue equation

TM mode	0	1	2
propagation angle Θ_i [deg]	83.42	76.76	69.91
k_{1x} [$\cdot 10^3$ m^{-1}]	62.7	125.5	188.2
γ [$\cdot 10^3$ m^{-1}]	538.2	527.1	508.1

Dispersion

Yet to be deduced are the group velocity, the group index and hence the dispersion relation in the $LiNbO_3$ waveguide. There are two types of dispersion: intra- and intermodal dispersion.
The intermodal dispersion originates from the difference in group velocity between miscellaneous modes, i.e. applying m in equation 1.22 resulting in various angles of propagation and therefore a variation in the group velocity and index. In contrast, intramodal dispersion occurs within every mode and can be separated into two parts once again; waveguide and material dispersion. The material of the guide may have refractive indices which vary with frequency, resulting in material dispersion. The former appears because the angle of propagation is frequency-dependent, since $k_{1_x}=k_0 n_1 \cos\Theta_i$ as obtained from the wave vector triangle in fig.1.11. Moreover, as clarified in equation 1.25, the penetration of the field into the medium 2, is likewise frequency-dependent because of the definition of γ yields $\gamma = \sqrt{k_z^2 - n_2^2 k_0^2}$.

By considering the finite penetration of the wave into the cladding leads to the so-called the

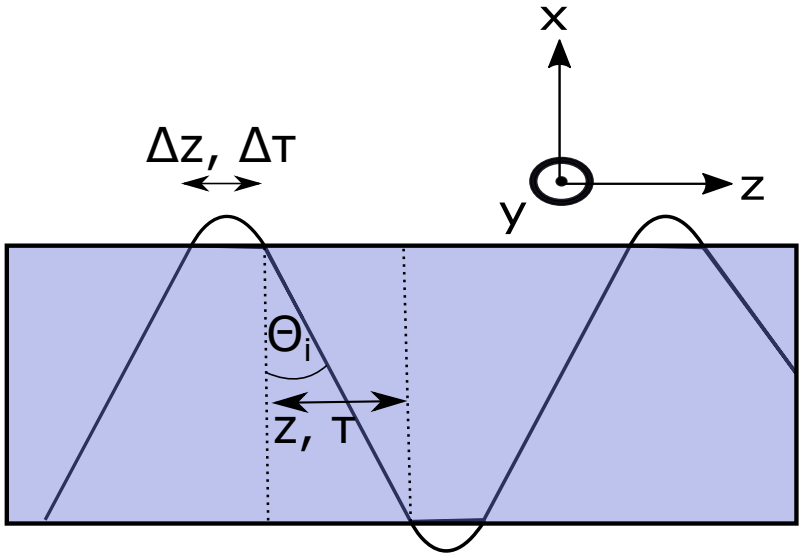

Figure 1.15.: Visualization of the contribution to phase shift between the reflected phonon-polariton waves: the penetration of the supporting material and cover by a wave propagating along the guide.

Goos-Hänchen shift. This is schematically depicted in fig.1.15, that summarizes the contributions to the phase shift that phonon-polaritons experience upon propagation in the waveguide contributes in addition to the propagation along the waveguide. An alternative, more mathematical derivation of the group velocity is given in the appendix A. Here I present a more schematic explanation.
Outgoing from fig.1.15 the group velocity yields:

$$v_g = \frac{\partial \omega}{\partial k_z} = \frac{z+\Delta z}{\tau+\Delta\tau}, \tag{1.26}$$

which can be re-written with the use of the calculation in the appendix A where the material dispersion is neglected since in fig.1.10b) the gradient of the blue graph, i.e. dispersion relation of phonon-polaritons in bulk of $LiNbO_3$ can be approximated linearly in the wave vector range 0 up to 300 rad/mm. From this I obtain the relation:

$$v_g = \frac{\partial \omega}{\partial k_z} = \frac{d \tan\Theta_i + (\partial\Phi/\partial k_z)}{(n_1 d/c\cos\Theta_i) - (\partial\Phi/\partial\omega)} \tag{1.27}$$

From equation 1.27 the group index n_{group} can be derived directly via v_g=c/n_{group} which results in the graph shown in fig.1.16a). The dispersion relation in b) can be calculated by integrating numerically over k_z, since the phonon-polaritons are propagating in the z-direction (cf. fig.1.12). By assuming the same electric field from equation 1.20 and by using the shorthand definition

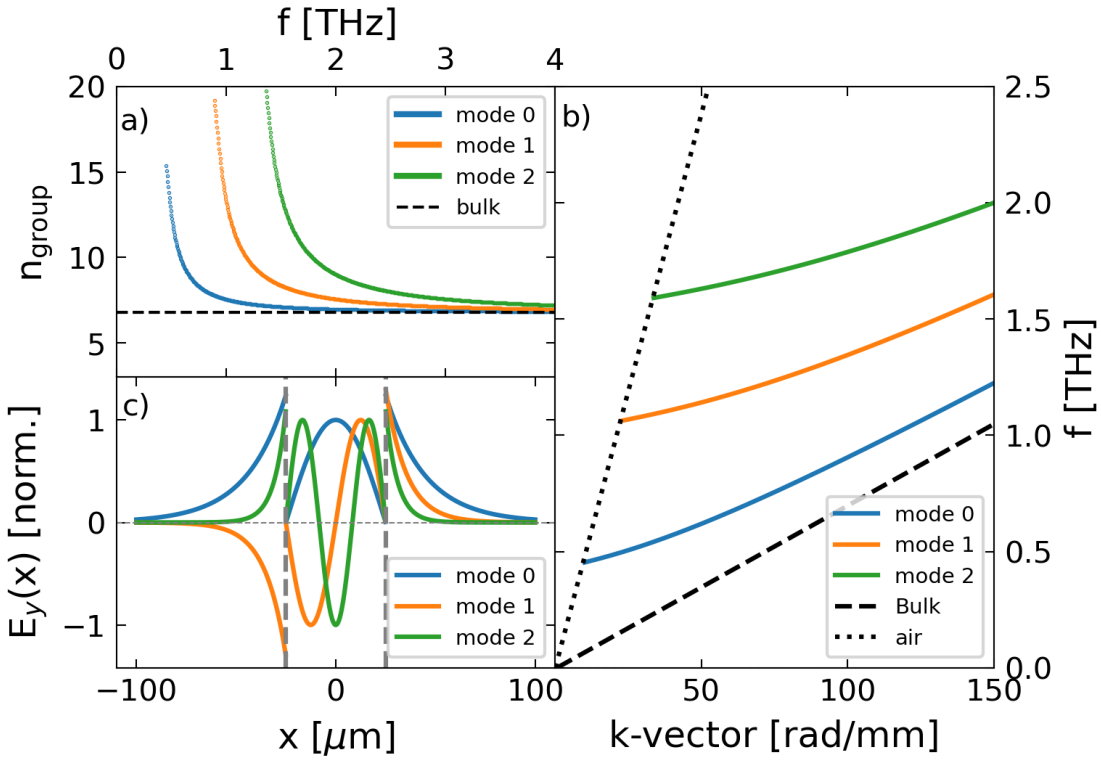

Figure 1.16.: Group index in a), dispersion relation in b) and the magnitude of electric field in y-direction inside and beyond the waveguide (represented as gray dashed lines) in c), for three transverse magnetic modes in a slab waveguide of $LiNbO_3$ of thickness 50μm compared to the dispersion relation in bulk of $LiNbO_3$ shown as dashed line.

$E_A(x)=E_0 e^{-\gamma x}$ the wave equation yields:

$$\begin{aligned} &\frac{\partial^2 E_y}{\partial x^2} + \frac{\partial^2 E_y}{\partial z^2} = \frac{1}{c^2}\frac{\partial^2 E_y}{\partial t^2} \\ \Leftrightarrow\ &\frac{\partial^2 E_A(x)}{\partial x^2} - k_z^2 E_A = -\underbrace{\frac{\omega^2}{c^2}}_{k_0^2}\frac{\partial^2 E_y}{\partial t^2} \\ \Leftrightarrow\ &\frac{\partial^2 E_A(x)}{\partial x^2} + (k_0^2 - k_z^2)E_A = 0. \end{aligned} \tag{1.28}$$

From the wave vector triangle trigonometry it is known that (k_0^2-k_z^2)=k_{1x}^2 applies in the core and (k_0^2-k_z^2)=-γ^2 in the cladding. Equation 1.28 then yields:

$$\frac{\partial^2 E_A(x)}{\partial x^2} + k_{1x}^2 E_A = 0, \text{ core}$$
$$\frac{\partial^2 E_A(x)}{\partial x^2} - \gamma^2 E_A = 0, \text{ cladding}$$

with the generic solutions:

$$E_A(x) = A\cos(k_{1x}x) + B\sin(k_{1x}x), \text{ core}$$
$$E_A(x) = Ce^{\gamma x} + De^{-\gamma x} \quad , \text{cladding}$$

In the core the cosine and the sine correspond to the even and odd modes m, which solution can be simplified to

$$E_A(x) = A\cos\left(k_{1x}x - \frac{m\pi}{2}\right) \tag{1.29}$$

In the region beyond the core I omit the nonphysical solution of an exponentially growing electric field, which would violate energy conservation. Thus, the solution in the cladding can be re-written to:

$$E_A(x) = \begin{cases} Ce^{\gamma(x+d)} & ,x < -d \\ De^{-\gamma(x-d)} & ,x > d \end{cases} \tag{1.30}$$

The electric field inside and beyond the waveguide must satisfy the boundary condition:

$$\frac{\partial E_y}{\partial x}\Big|_{x=\pm 25\mu m} = \text{const.}$$

This is used to extract the magnitude of the constants A, C and D in order to plot the field distribution shown in fig.1.16c) for the different modes inside and outside the waveguide. The paper by Yang et al.[10] shows a similar derivation for TE-modes.

2. Setup and data analysis

Excitation and detection of sub-picosecond signals with THz frequency components, have become possible using femtoseconds-laser pulses that are often derived from Ti:Sapphire laser. The group of Keith Nelson at MIT has introduced the phase mask interferometer as an efficient way to generate a transient grating excitation in the sample [35]. This setup allows exciting quasiparticles at the sample spot with a well-defined wave vector, e.g. generate selectively excited phonon-polaritons if the sample is a ferroelectric material. The book of Pohl [36] discusses laser-induced gratings in more detail.
This chapter contains a description of the experimental setup and explains the pump-probe experiment. At first, I discuss the data-analysis routine based on a measurement of the frequency-resolved optical gating experiment (FROG) on a thin SiO_2 microscopy slide, in contrast to the additional signatures that arise due to the presence of the phonon-polaritons in $LiNbO_3$.

2.1. Experimental setup

Fig.2.2 shows a sketch of the setup that is described in the following.
The mode-locked Ti:Sapphire oscillator laser produces pulses, with a spectrum that is 8 nm broad, centered at the wavelength 806 nm, as shown in fig.2.1 where also the spectrum of the laser in cw mode and the spectrum of the amplifier is depicted. This corresponds in theory to a Fourier limited pulse of the oscillator of 120 fs length. The average power of the oscillator laser amounts

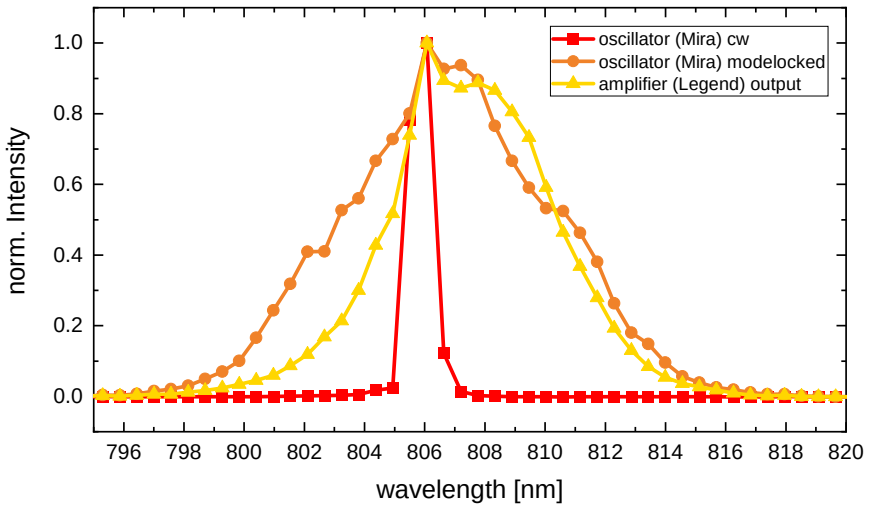

Figure 2.1.: Normalized spectra of the Ti:Sapphire oscillator laser in cw and mode-locked mode. The amplifier output is also shown.

to 400 mW and the repetition rate is approximately 80 MHz resulting in a small pulse energy of approximately 5 nJ. To study the fluence dependence of the phonon-polariton generation up to a potentially non-linear regime, I require larger pulse energies. Thanks to the development of the chirped pulse amplification technique by Strickland et al. in the 1980s, pulses with few mJ or even more can be generated. In this experiment, I employ pulses with an energy of roughly 0.4 mJ per

pulse at a repetition rate of 1 kHz, resulting in an average power of 400 mW. The actual power that arrives at the sample is reduced as the pulses traverse the setup because of material absorption and intended reflection at the polarizer-wave plate combination that is used to vary the intensity of the beam.
The amplified laser pulses cover a spectral range with a bandwidth of FWHM = 5.7 nm centered at approximately 807 nm, resulting in a Fourier limited temporal width $\tau_{F,FWHM}$ of approximately

$$\tau_{F,FWHM} = \frac{2\ln 2}{\Delta\nu} = \frac{2\ln 2 \cdot \lambda^2}{c\Delta\lambda} = 160\text{fs} \tag{2.1}$$

The actual pulse length is determined in a transient grating frequency-resolved optical gating (TG-FROG) experiment discussed in section 2.2.
At the entrance of the setup, the polarizer is set so that only light that is polarized parallel to the table enters the setup. Afterwards I employ a Galilean lens telescope that reduces the beam diameter

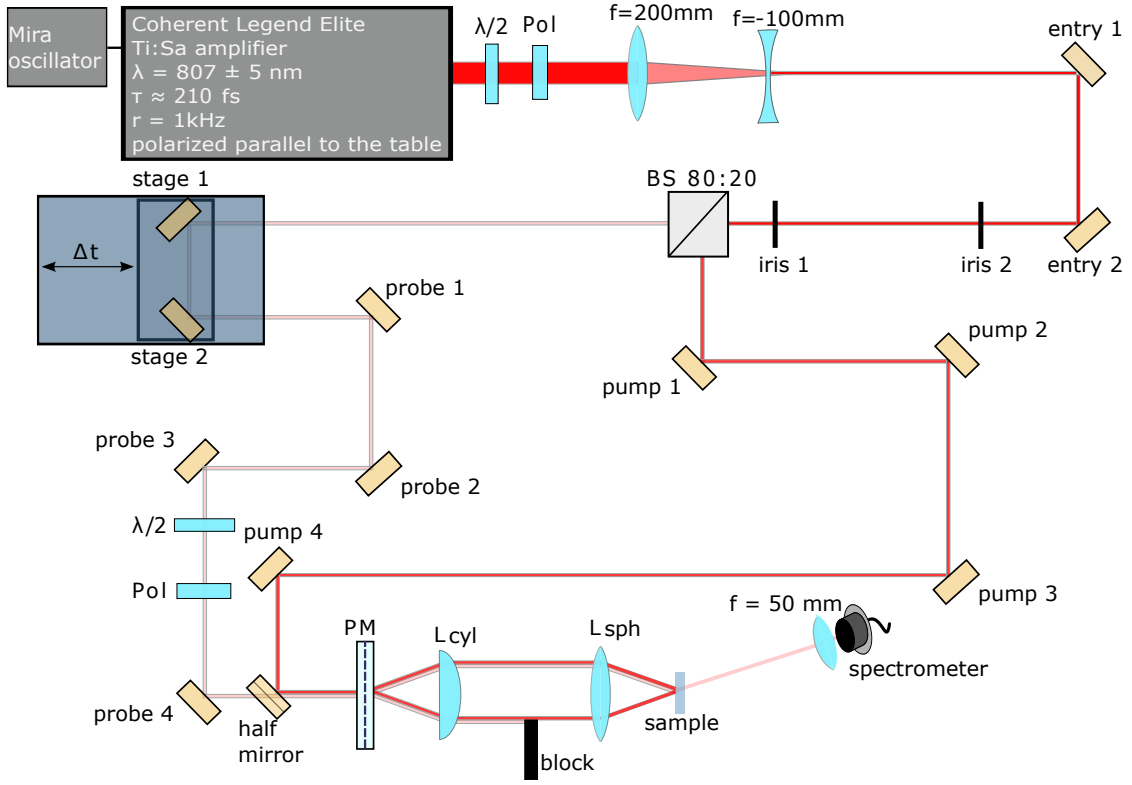

Figure 2.2.: Sketch of the experimental setup

to approximately 1 mm x 1 mm, in order to be able to fit a pump and a probe beam through the 5 mm x 5 mm transmission gratings. The beamsplitter (BS) divides the incoming 800 nm pulses into two parts with a reflection/transmission ratio of 80/20. The reflected part acts as the pump beam and the transmitted part serves as the probe beam. The probe beam traverses a delay stage, where the beam may be delayed by up to 150 ps. To implement a modifiable intensity change of the probe beam, another system of wave plate and polarizer is added, right after the mirrors probe 2 and probe 3 that shift the beam 2 mm upwards. Subsequently, the pump and probe beam gather and propagate through a 5 mm x 5 mm phase mask grating. The phase mask is designed for an efficient diffraction of the first order. Residual higher and lower orders of diffraction are blocked, which results in an additional loss of energy. By measuring the intensity before the phase mask and at the sample position, the loss can be estimated to about 20%, i.e. 80% will arrive to the sample spot. In the following chapter, only the values incident on the sample are discussed. The cylindrical lens

has a focal length of f_1=75 mm, the spherical a focal length of f_2=100 mm.
The separated four beams, two for pump and probe beam each, are shown in fig. 2.3, that depicts the so-called box-CARS geometry [37]. The scattered beam in the k_3-direction is detected by the

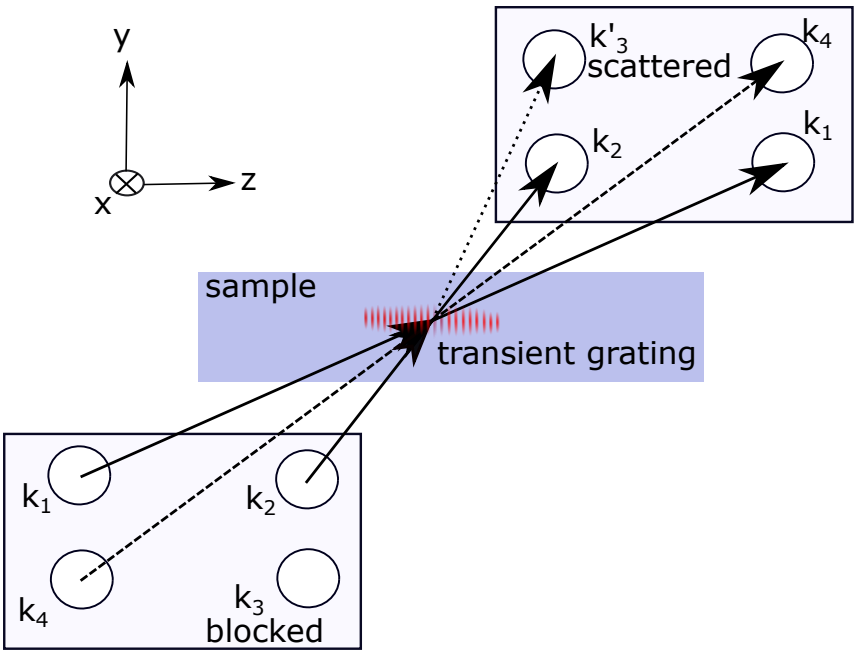

Figure 2.3.: Sketch of box-CARS geometry, used for the following four-wave mixing experiments; $\mathbf{k}_1$ and $\mathbf{k}_2$ interfere at the translucent probe to produce a transient grating, where $\mathbf{k}_4$ is diffracted to the direction of $\mathbf{k}_3'$ by ISRS.

fiber-optic spectrometer USB4000 by OceanOptics that contains a blazed grating CCD line array made of 3648 pixels. The spectral range is roughly 650 nm up to 1300 nm resulting in a resolution of $\delta\lambda$ =0.2 nm in the region of interest around 800 nm. To capture as many diffracted photons as possible, a focussing lens is placed in front of the spectrometer fiber. It is an advantage of the box-CARS geometry that the diffracted signal is spatially displaced from the pump pulses, which reduces the background to the signal from the pump light, thus increasing the signal. For adjusting the detector position, we can open the normally blocked beam $\mathbf{k}_3$, which indicates the direction in which the diffraction of $\mathbf{k}_4$ occurs.

2.2. Description of measured data

In the following, the analysis of data taken by the camera and spectrometer are shown and discussed for one representative example.
In this thesis, I employ an area camera (model Basler acA4024-8g) in order to visualize the pump spot. This camera has a small pixel size of 1.85 μm x 1.85 μm. It is also used to determine the area of the pump and probe beam at the sample position, which is necessary for the calculation of the excitation fluence F. The camera is placed at the sample spot instead of the specimen and measures the intensity profile of strongly attenuated beams. The intersecting pump beams, and the remaining probe beam, are depicted and analyzed in fig.2.4. By doing the Fourier transformation of the induced transient spatial modulation signal in fig.2.4(a) I find a wavelength of 77.9 μm for the modulation of the intensity.
The FWHM from fig.2.4(a) and fig.2.4(b) averages to approximately 60μm in height and 830μm in length, resulting in an approximated elliptical area A = π FWHM$_x$/2$\cdot$ FWHM$_y$/2 ln(2)$^{-2}$= 8.14$\cdot$

$10^{-4}(\mathrm{cm})^2$.

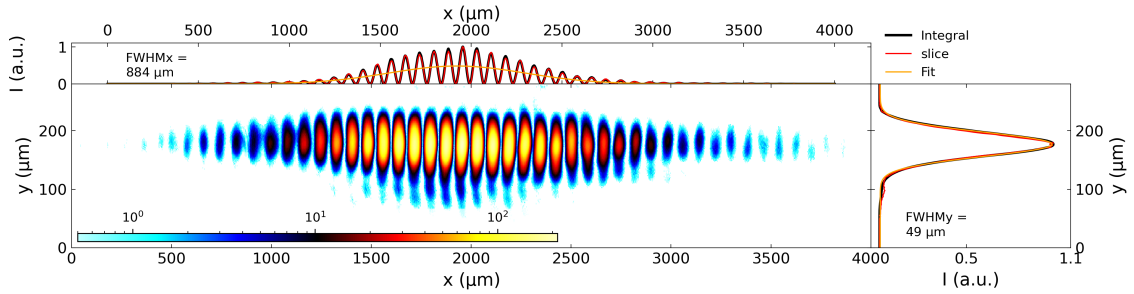

(a) Two pump pulses intersect resulting in spatial modulation of the excitation intensity that is detected with a CCD camera, FWHM in height = 49 μm, FWHM in length = 884 μm

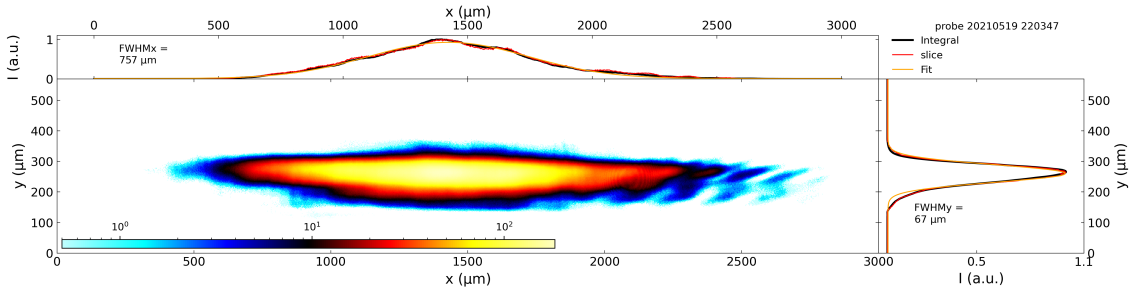

(b) Single probe pulse detected with a CCD camera, FWHM in height = 67 μm, FWHM in length = 757μm

Figure 2.4.: Representative beam profile of a) the pump and b) the probe pulse used in the transient grating experiments at the sample spot and visualization of the intensity profile. A cut along the longitudinal- (y-axis) and transverse-axis (x-axis) is provided besides the pattern in order to estimate the beam dimensions. Both pump and probe pulses pass the same optics made of a phase mask grating a cylindrical lens and a spherical lens before intersecting at the focal spot. This leads to their comparable spatial dimension.

Pulse characterization using TG-FROG

Having considered the beam profile taken by the CCD camera, the focus is upon the measured data from the spectrometer. First, I will consider glass as a sample, to measure the TG-FROG, afterwards the frequency resolved data measurement from $LiNbO_3$ is shown. In order to control and measure the spectral chirp and the pulse duration, I applied the TG-FROG [38] method. The result is depicted in fig.2.5. The utilized sample was a thin microscopy slide made of amorphous quartz glass (SiO_2), which does not show phonon-polariton excitations, that could distort the signal from the electronic quasi-instantaneous response. The delay time 0 ps is set to the point in time when the diffraction of the probe beam $\mathbf{k}_4$ from the transient intensity grating generated by the pump beams $\mathbf{k}_1$ and $\mathbf{k}_2$ is largest. The four-wave mixing process described in section 1.2.1 and shown in fig.2.3 results in an additional factor to calculate the actual pulse length τ_P. From the diffracted probe intensity signal S, that is measured by the spectrometer one can extract the pulse length as described by Trebino et al. [39] via:

$$S \propto |\int_{-\infty}^{\infty} e^{-i\tau\omega} E_{\mathrm{signal}}(t-\tau)|E_{\mathrm{gate}}(t)|^2 d\tau|.$$

Therein I assume that the electric field of the probe pulses $E_{gate}(t)$ and the pump pulses $E_{signal}(t)$ share the same time-dependence. By considering

$$E \propto e^{-\frac{t^2}{2\sigma_P^2}} \Rightarrow S \propto e^{-\frac{t^2}{3\sigma_P^2}}$$

the ratio of the standard deviation of the pulse σ_P and signal detected via FROG-measurement σ_{FROG} can be derived via

$$S \propto e^{-2\frac{t^2}{3\cdot 2\sigma_P^2}} \stackrel{!}{=} e^{-\frac{t^2}{2\sigma_{FROG}^2}}$$
$$\Rightarrow \sigma_{FROG} = \frac{\sigma_P}{\sqrt{\frac{2}{3}}}. \tag{2.2}$$

The ratio of the FWHM (τ) and standard deviation (σ) yields $\tau/\sigma = 2\sqrt{2\ln(2)}$. With the use of equation 2.2 the actual pulse length τ_P can be derived by extracting $\tau_{FROG} = 257\,fs$ from fig.2.5 :

$$\tau_P = \frac{\tau_{FROG}}{\sqrt{\frac{3}{2}}} = 210\,fs \tag{2.3}$$

In fact, one can perceive a slight spectral chirp in fig.2.5 which may explain the difference according to the calculated values between the theoretical Fourier limit in equation 2.1 and the measured pulse length in equation 2.3.
Since the excitation of phonon-polaritons is an impulsive process, only phonon-polaritons with a frequency less or equal to $1/\tau_P = 4.76\,THz$ with the pulse length derived in equation 2.3 are excited efficiently.

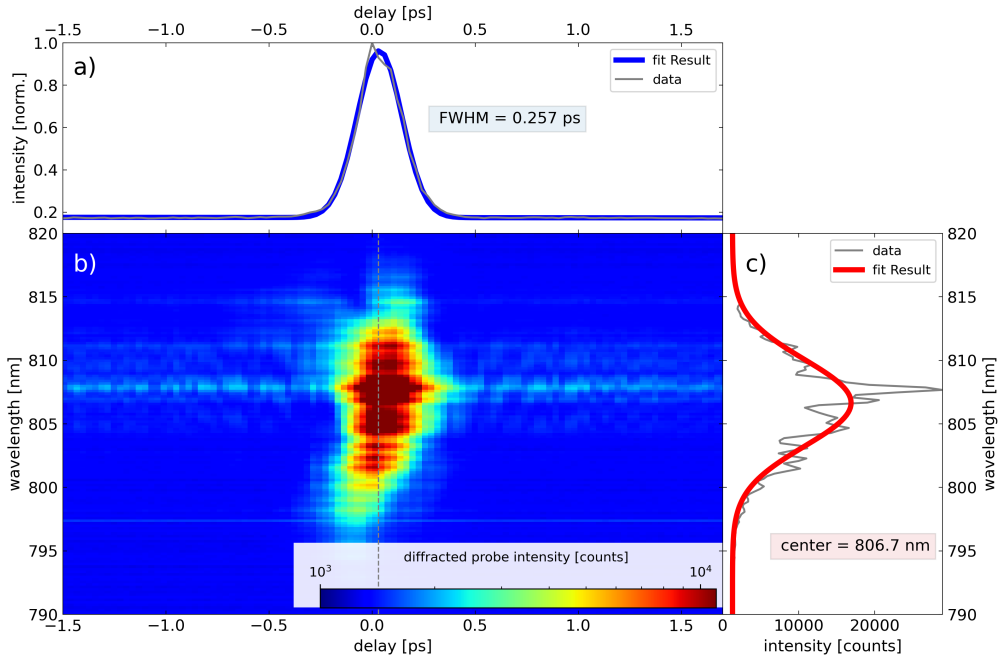

Figure 2.5.: In b) the TG-FROG signal for the above-mentioned four-wave mixing pulses is recorded with the spectrometer for different pump-probe delays. In panel c) a vertical cut at 0 ps is presented and a Gaussian fit yields center and FWHM in the spectral range. In the top panel, a) the spectrally integrated diffraction intensity from 795 nm up to 815 nm is shown. Gaussian fits to the spectrum and the time-trace are used to analyze the data in c) and a) respectively.

Analysis of frequency resolved data from $LiNbO_3$ measured by spectrometer

In fig.2.6 the data taken by the spectrometer of bulk $LiNbO_3$ excited by a transient grating with wavelength λ_{tg}=77.9 μm, is depicted. In addition to the TG-FROG feature at t=0 one observes an

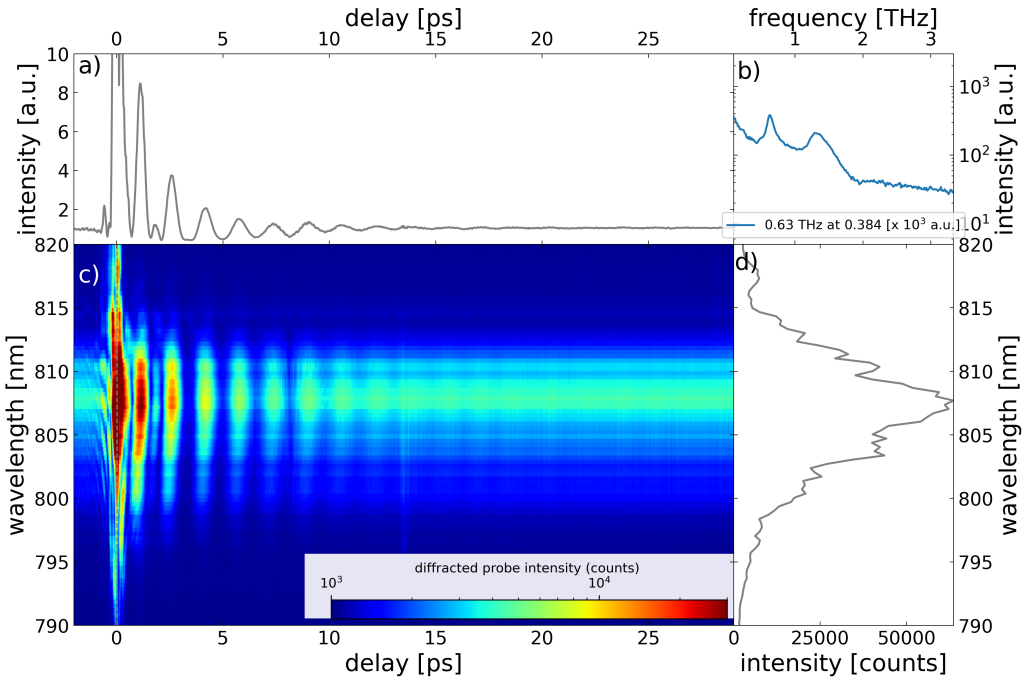

Figure 2.6.: Representative time-dependent spectrum of the diffracted probe intensity in a transient grating excitation experiment on bulk $LiNbO_3$. The oscillations in the diffraction intensity result from the excitation of phonon-polaritons. The parameters for pattern a) and d) applies from fig.2.5, i.e. d) shows the vertical cut of pattern c) at t = 0 ps and a) represents spectrally integrated diffraction intensity from 795 nm to 815 nm

oscillation after 0 ps, visible in the colorized intensity pattern in c). The vertical d) and horizontal a) sections arise similarly as described in fig.2.5. Panel b) shows the Fourier transform of the time-dependent diffraction signal shown in a), and the frequency ν=0.63 THz with the maximum Fourier amplitude is stated. Thereby, each wavelength in the region of interest is Fourier analyzed individually, before summing all contributions. Thus, if there is any phase difference between different wavelengths due to the chirp mentioned in fig.2.5, the frequency does not undergo a shift.

Analysis of the time resolved plot for different wavelengths

The wavelength range in fig.2.5 and fig.2.6 represents the relevant range in which phonon-polaritons are detected. A time resolved plot for different wavelength for the measurement in fig.2.6 is presented in fig.2.7. By considering the data for every wavelength, in the range from 795 nm up to roughly 815 nm oscillations are visible. The integral over the range is also shown. In the following discussion, I will only show and discuss the integrated spectral intensity

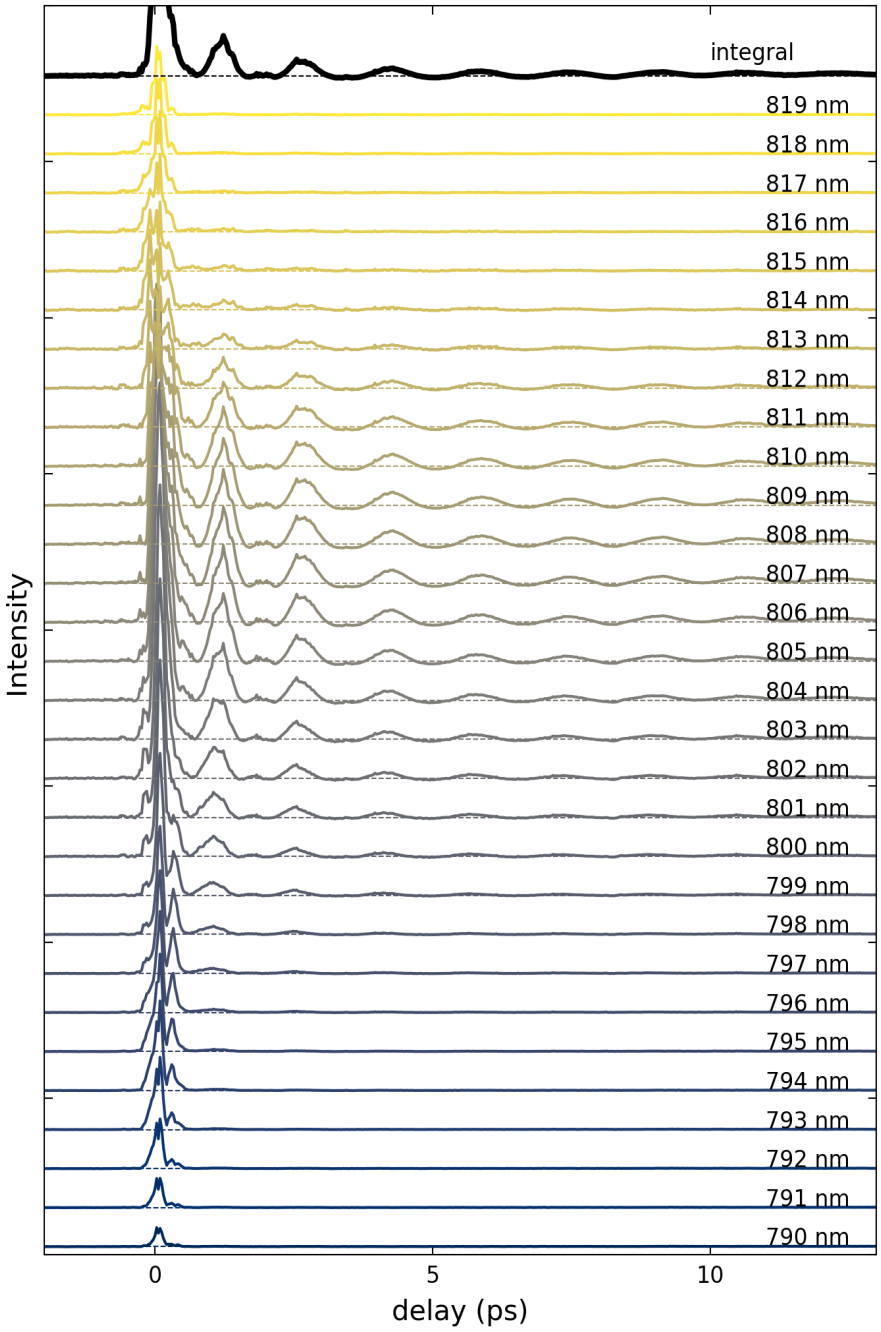

Figure 2.7.: Time-resolved analysis at individual wavelengths in the range from 790 nm up to 820 nm for bulk $LiNbO_3$. This underlines that oscillations of the diffraction intensity are visible mainly from 795 nm - 815 nm, which is the wavelength range used in further evaluations. This data set is the same as shown in fig.2.6

3. Results and Discussion

This chapter contains a set of systematic measurement series and their analysis. I present a fluence-dependent study, a rotation series of the sample and a measurement series where the sample is displaced with respect to the pump. For each experiment, I compare the bulk $LiNbO_3$ and the response of the 50 μm thin $LiNbO_3$ waveguide sample. Both samples are fabricated in x-cut. The measured frequencies and calculated wave vectors for the bulk and waveguide modes are compared to the dispersion relations.

3.1. Fluence series of the pump beam

By adjusting the wave plates shown in fig.2.2 the power of the pump beam can be varied by simultaneously maintaining the power of the probe beam constant and vice versa. The fluence F of the excitation and detection beam is defined as F = E / A, where E is the energy of a pulse incident on the sample (confer section 2.1) and calculated via E = P / r. Here, r is the repetition rate of the laser and P the average power incident at the sample. The elliptical area A = $8.14 \cdot 10^{-4}$ $(cm)^2$ calculated in section 2.2 applies for the probe and pump beam likewise.

3.1.1. Homodyne detection effects

The signal detected by the spectrometer at one specific wavelength, i.e. one definite pixel of the spectrometer detecting the electric field E_3, is composed of three components depicted in fig.3.1 [21, chapter 5]. The incident beam $\mathbf{k}_4$ scatters from the right, respectively left propagating phonon-polaritons. These wave vectors are indicated as anti-Stokes scattering k_4^+ (or E^+), respectively Stokes-scattering k_4^- (or E^-). In fact, the probe beam also scatters from impurities or inhomogeneities in the sample, where no momentum transfer occurs. This results in an elastic Rayleigh scattering contribution E^{ela} to the electric field signal E_S at each pixel of the spectrometer. Thus, the detected signal intensity at the spectrometer position results from the superposition of three contributions:

$$\begin{aligned} E_S &= E^{\text{ela}} + E^+ + E^- \\ \Rightarrow I_S &= |E^{\text{ela}} + E^+ + E^-|^2. \end{aligned} \tag{3.1}$$

In the following I consider three cases: $E^+ \approx E^- \approx E^{ela}$, $E^+ \approx E^- \gg E^{ela}$ and $E^{ela} \gg E^+ \approx E^-$. The electric fields are given by the initial magnitudes E_0, damping rate γ, delay time of the probe beam τ and a scattering phase $\Phi_\pm = \pm\omega_{PP}\tau$: ω_3' represents the corresponding frequency to the wave vector k_3'.

$$\begin{aligned} E^+ &= E_0^+ e^{-\gamma\tau} e^{i(\omega_{4+}+\omega_{PP})t+\Phi_+} = E_0^+ e^{-\gamma\tau} e^{i(\omega_3')t+\Phi_-} \\ E^- &= E_0^- e^{-\gamma\tau} e^{i(\omega_{4-}-\omega_{PP})t+\Phi_-} = E_0^- e^{-\gamma\tau} e^{i(\omega_3')t+\Phi_-} \\ E^{\text{ela}} &= E_0^{\text{ela}} e^{-\gamma\tau} e^{i(\omega_3')t} \end{aligned}$$

An extended derivation for every case is presented in the PhD thesis of Goldshteyn [21, appendix

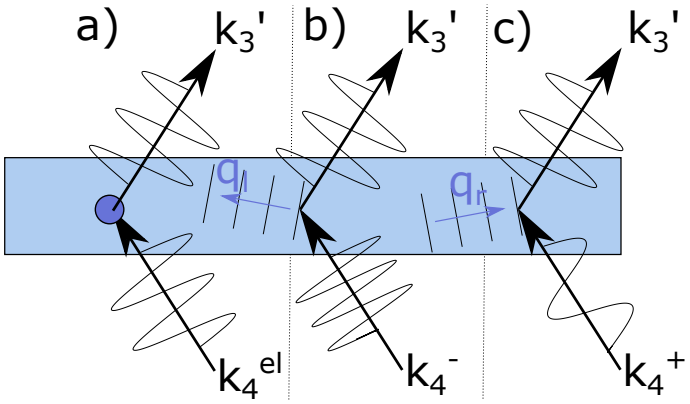

Figure 3.1.: Sketch of three different components of the electric field contributing to the signal detected by the spectrometer at a specific wavelength. Different wavelength components of the incident beam $\mathbf{k}_4$ contribute to the electric field E_3 on a pixel along $\mathbf{k}_3'$ are a) diffracted by impurities, b) left propagating phonon-polaritons or c) right propagating phonon-polaritons in $\mathbf{k}_3'$-direction

A.1].
A mixed term $|E_0^- \cdot E_0^+|$ states $I_0^\pm$, thus equation 3.1 can be re-written for the case $E^+ \approx E^- \gg E^{ela}$

$$I_S' = |E^+ + E^-|^2$$
$$I_S' = 2I_0^\pm(1-\cos(2\omega_{PP}\tau))e^{-2\gamma\tau} \tag{3.2}$$

In contrast, the case $E^+ \approx E^- \approx E^{ela}$ yields the more complicated form for I_S'', where I_0^{ela}, $I_\pm^{ela}$ and $I^\pm$ are mixed terms of magnitudes of the electric fields

$$I_S'' = |E^{ela} + E^+ + E^-|^2$$
$$I_S'' = I_0^{ela} - 4I_\pm^{ela}e^{-\gamma\tau}\sin(\omega_{PP}\tau) + 4I^\pm e^{-2\gamma\tau}\sin^2(\omega_{PP}\tau). \tag{3.3}$$

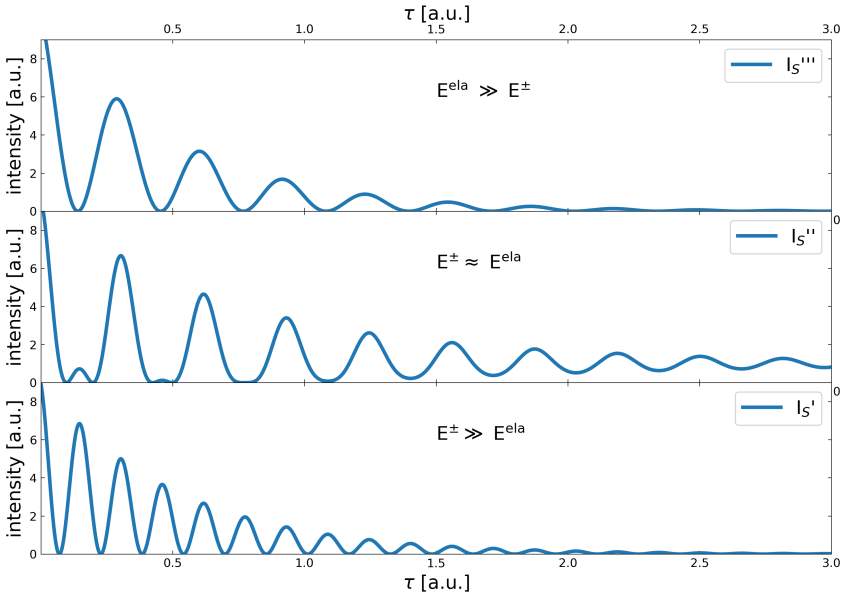

Figure 3.2.: Magnitude of the intensity of the signal incident at the spectrometer for three different cases indicated in equation 3.2,3.3 and 3.4. with arbitrary parameters

The third case $E^{ela} \gg E^\pm$ has two possible origins. A residual electric field with wave vector $\mathbf{k}_3$ incident at the spectrometer, either because it is not perfectly blocked or by using a neutral density

filter as described in [20] or because the probe beam $\mathbf{k}_4$ and maybe both excitation beams $\mathbf{k}_1$ and $\mathbf{k}_2$ are scattered at impurities and the surface of the sample. The magnitude of E^{ela} can then be large. It is not determined in the thesis which effects apply for this work. In contrast, the magnitude of $E^{\pm}$ decreases if less phonon-polaritons are excited, e.g. because the excitation pulses contain a low fluence, so that less photons may excite phonon-polaritons through ISRS. Thus also increases the importance of E^{ela}. The intensity yields with the mixed term $I_{\pm}^{ela}$ of the magnitudes of the electric fields $E^{\pm}$ and E^{loc}

$$\begin{aligned} I_S''' &= |E^{ela} + E^{+} + E^{-}|^2 \\ I_S''' &= I_0^{ela} + 2I_{\pm}^{ela}\cos(\omega_{PP}\tau)e^{-\gamma\tau} \end{aligned} \tag{3.4}$$

The intensities of the simulated signals for all three cases are shown in fig.3.2 for different relative scaling of E^{+}, E^{-} and E^{ela}.
Here I discuss the measurements of the fluence series for the pump beam.
The integral over all wavelengths from 795 nm up to 815 nm (cf. fig.2.6) is plotted for different fluences in fig.3.3 and fig.3.5. For every fluence, a dashed line shows the respective initial intensity at -2ps delay time. The Fourier analyzed data corresponding to the time resolved data is depicted in fig.3.4 and fig.3.6. For the fluence series for both samples, the phase mask pattern has a spatial period of λ_{PM}=114.8 μm. The fluence of the probe beam is constantly 7 mJ/(cm)^2, except for pump fluences below 35 mJ/(cm)^2. For these cases, the fluence of the probe beam yields one fifth of the fluence of the pump beam since the beamsplitter has a fixed transmission/reflection ratio of 20% so that a constant probe intensity could not be maintained. The beam profile for this measurement series is provided in the appendix C.

3.1.2. $LiNbO_3$ bulk

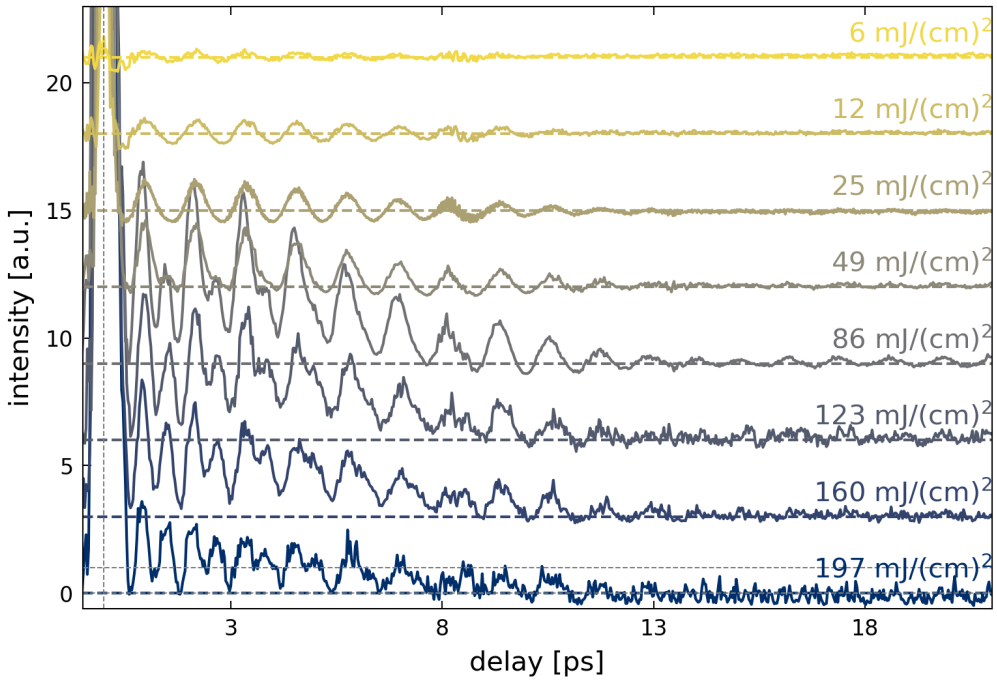

Figure 3.3.: Time resolved data of excitation beams with different fluences for bulk $LiNbO_3$

For low fluences, i.e. 6 mJ/(cm)^2 up to 25 mJ/(cm)^2, the plot in fig.3.2 corresponding to $E^{ela} \gg E^{\pm}$ describes the data in fig.3.3 quite well. Only the frequency of the phonon-polaritons occurs in the

Fourier analysis, fig.3.4, while the second harmonic is absent. For higher fluences, 49 mJ/(cm)^2 up to 197 mJ/(cm)^2 a second peak in the Fourier analysis emerges at a frequency that is twice the frequency of the phonon-polaritons that equals the frequency that is obtained for low fluences. By increasing the fluence of the pump beam, the intensity of the second peak increases. For fluence around 100 mJ/(cm)^2 the approach $E^{ela} \approx E^{\pm}$ fits better to the qualitative structure of the measured signal whereas the time resolved data for 197mJ/(cm)^2 corresponds to $E^{\pm} \gg E^{ela}$. Since the electric field E^{ela} is determined by the probe pulse scattering at impurities in the sample this component should remain constant. A comparison of the intensity of the signal at the peak frequencies results into a signal amplitude depending on the fluence plot in fig.3.4. As described above, the intensity of the second peak at 1.69 THz increases with increasing fluence. On the contrary, the first peak at 0.85 THz increases from 6 mJ/(cm)^2 to 50 mJ/(cm)^2 and decreases afterwards. That effect originates in two reasons; The high fluence enables a non-linear process, three-photon absorption, which is unlikely for low fluences [40]. Since ISRS is an inefficient process, the non-linear influences the signal amplitude strongly, expresses in a decrease of the signal amplitude for the lower frequency. Upon decreasing the fluence, further non-linear effects may also affect the second order FFT peak at 1.69 THz. Secondly, the scattering of the pump beams on impurities may become more relevant and increase the time-independent background relative to the phonon-polariton contributions in the spectrometer.

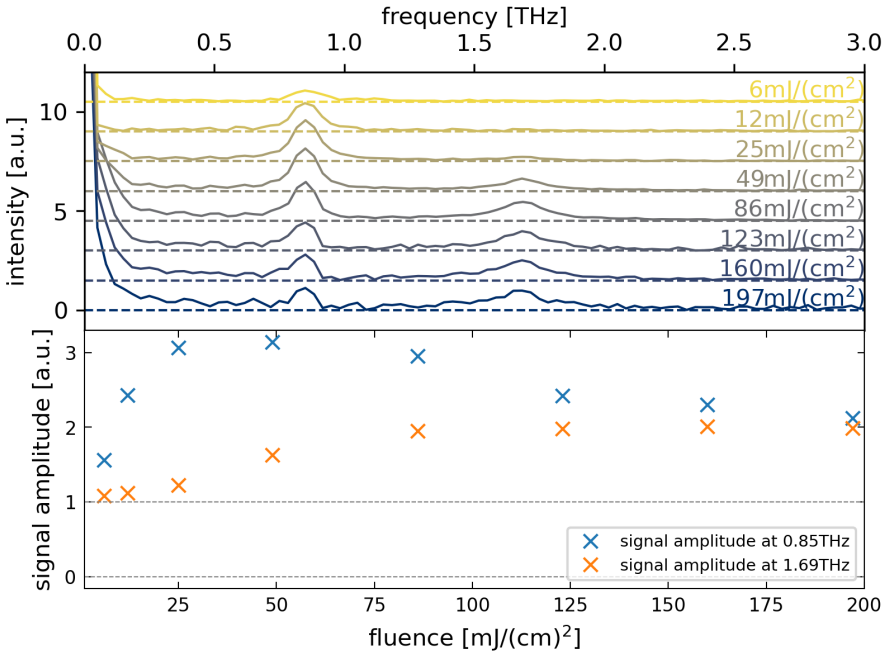

Figure 3.4.: Fourier analysis of the time resolved data from t=0.6 ps to 26 ps for different fluences of the pump beam in bulk $LiNbO_3$ and the signal amplitude at selected frequencies.

3.1.3. $LiNbO_3$ waveguide

For the waveguide, the same experiment with comparable fluences was implemented for comparison. As derived in chapter 1 one expects multiple waveguide modes to be excited in a thin slab. The superposition of these signals leads to the more complex shape of the oscillations in the fluence series shown in fig.3.5. In contrast to the bulk measurement, with increasing fluence, an additional peak at twice the frequency of a single mode does not occur, but three transverse magnetic waveguide modes (m=0,1,2) and two transverse electric waveguide modes (m=0,1) are

excited, the signal of the zeroth TM mode superimpose with the signal of the first TE mode in the Fourier analysis. The transverse electric modes may occur because the c-axis of the waveguide sample is not parallel to the propagation direction of the phonon-polaritons but slightly tilted ($\leqq 5°$), as described in [10]. Since the excitation of transverse electric modes was not intended, I will only discuss the transverse magnetic modes in the following. The transverse electric modes indicated at 0.68 THz and 0.8 THz are marked in fig.A.1. However, the signal amplitude increases nearly linearly with increasing fluence, as depicted in fig.3.6.

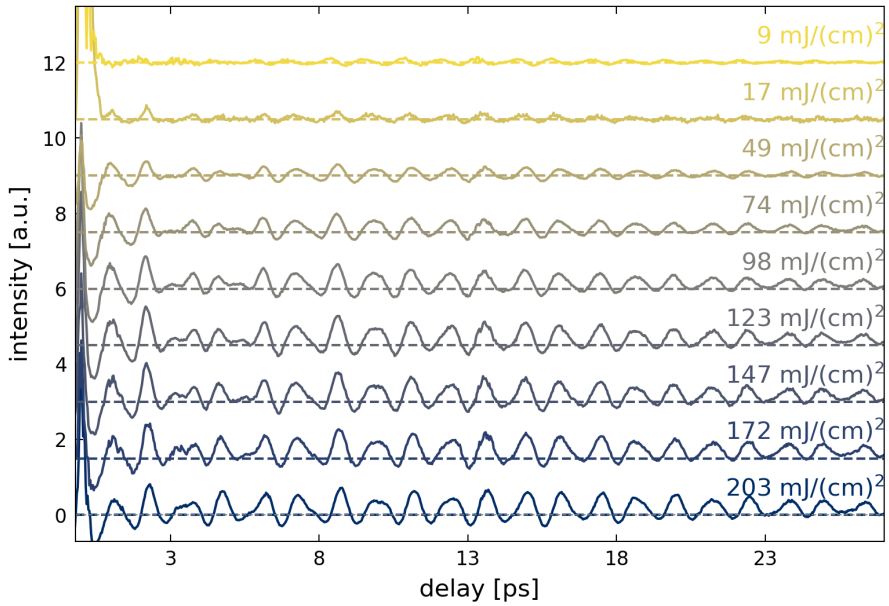

Figure 3.5.: Time resolved data of excitation beams with different fluences for waveguide $LiNbO_3$ with a transient grating wavelength of 77.9μm.

Since the waveguide thickness is limited by 50 μm, the interaction volume between the probe and the pump beam is finite. Thus, less phonon-polaritons are excited in the waveguide in total compared to the bulk because of the smaller interaction volume, so $E^{\pm}$ is much smaller and hence $E^{\text{ela}} \gg E^{\pm}$. Simultaneously, the beams scatter at the surface as they do in the bulk such that the elastic contribution to the electric field E^{ela} is not as strongly affected from the confinement of the waveguide, thus the case $E^{\text{ela}} \gg E^{\pm}$ applies for the waveguide.
By comparing the time resolved data for the bulk with the time resolved data for the waveguide in fig.3.5 the long-lasting phonon-polariton oscillations are remarkable. In case of the bulk specimen, the phonon-polariton wave packet propagates into the depth of the bulk according to the direction of propagation calculated in section 3.4 and derived in section 1.2.2. At a delay time of the probe pulse of 25 ps the oscillations in the waveguide are still apparent and the varying electric field approaches one specific frequency. More detailed discussed in section 3.3.
In the Fourier analysis for the higher frequency in bulk at 1.69 THz and three transverse magnetic modes (m=0,1,2) in waveguide at high fluences, a saturation of the signal amplitude occurs. Thus, I also observe a saturation of the phonon-polariton generation in the waveguide, that may arise from the onset of three-photon absorption processes [40]. The time resolved data for the waveguide fig.3.5 show a significantly smaller than the corresponding bulk signal in fig.3.3. The phonon-polaritons propagate much further parallel to the sample surface in the waveguide as compared to the bulk specimen. This may be due to the large contribution of the evanescent THz field that propagates outside the waveguide, as shown in fig.1.16c), which experiences no damping to lattice

vibrations.

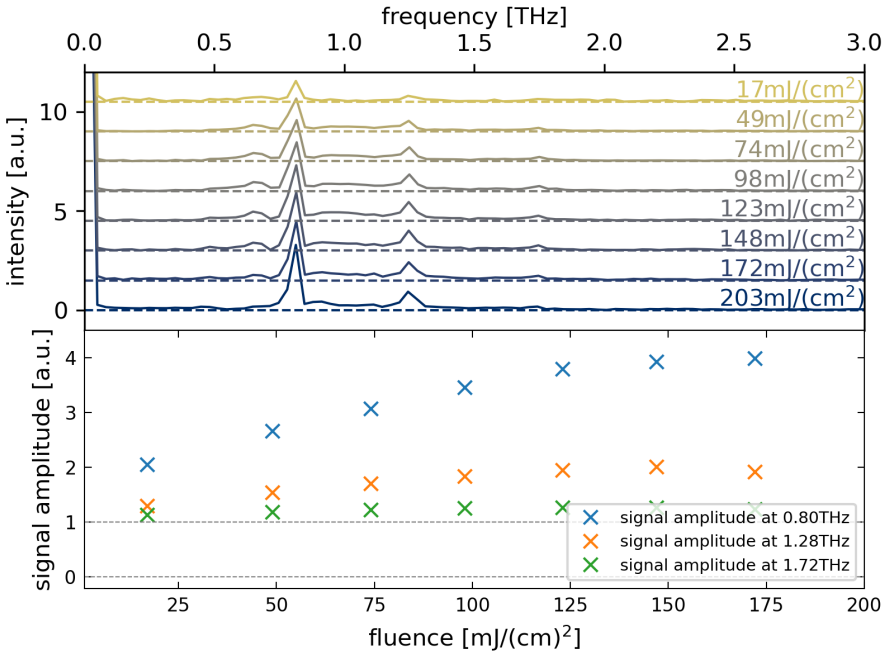

Figure 3.6.: Fourier analysis of the time resolved data from t=0.6 ps to 26 ps for different fluences of the pump beam in waveguide $LiNbO_3$ and the signal amplitude at selected frequencies.

3.2. Rotation series in bulk and waveguide

For the bulk and the waveguide, the samples were rotated as depicted in fig.3.7. Thus, the c-axis described in section 1.3 is rotated by the angle Θ_{rot} with respect to the z-component of the wave vector of the phonon-polaritons. If the incident light beams are polarized parallel to the c-axis, the excitation and detection of phonon-polaritons is highly efficient since the polarizability for the modes excited by light polarized parallel to the c-axis is roughly ten times higher compared to terms with a mixed polarizability, i.e. a tilted c-axis * [41], [42].

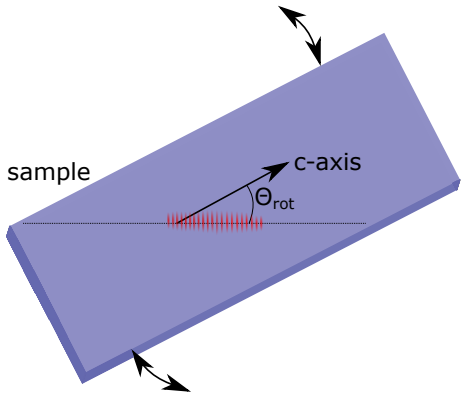

Figure 3.7.: Description of the method to measure rotation series in bulk and waveguide. The angle of rotation Θ_{air} is varied by turning the whole sample and thus the c-axis. The orientation of the transient grating excitation remains fixed.

*respectively light with a non-zero part polarized transverse to the c-axis which does not apply for this thesis

I present the data in a similar manner as in section 3.1 and compare the bulk $LiNbO_3$ and the slab waveguide. The beam profile for the pump and probe beam is provided in the appendix C. For the rotation series, the phase mask pattern is set to $\lambda_{PM} = 38.3\mu m$.

3.2.1. $LiNbO_3$ bulk

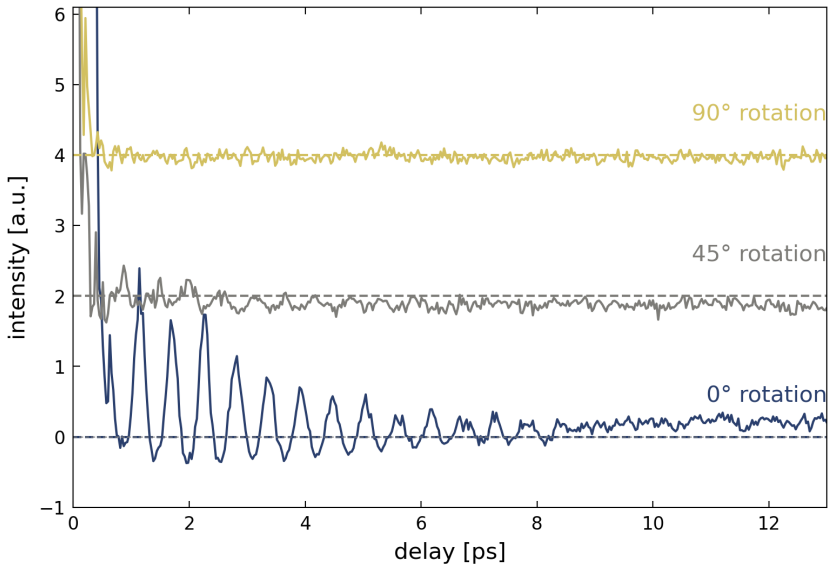

(a) Time resolved data for different rotation angles of the sample in bulk $LiNbO_3$.

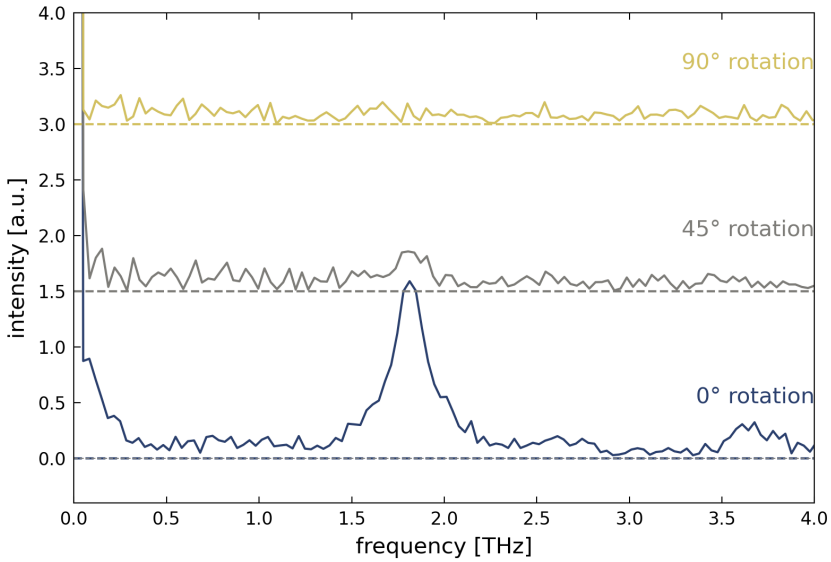

(b) Fourier analysis of the data from t=0.6 ps to 13 ps at different rotation angles of the sample in bulk $LiNbO_3$

Figure 3.8.: [Time resolved data and Fourier analysis for different rotation angles of the sample in bulk $LiNbO_3$.The wavelength of the transient grating is $\lambda_{tg} = 26.2\,\mu m$, the fluence of the pump yields 86 mJ/(cm)^2 and for the probe beam 7 mJ/(cm)^2.

Since the polarizability decreases with tilted c-axis as described above, the oscillations of the intensity $\propto |E|^2$ shown in fig.3.8(a) decreases proportional with increasing rotation angle.

The relation between polarizability and dielectric function was derived in section 1.4, more precisely equation 1.10 and equation 1.11. With decreasing polarizability, the modified oscillator strength (eq.1.13) decreases, leading into a disappearance of the magnitude of the oscillation. This is in qualitative agreement with the Fourier analysis presented in fig.3.8(b).

3.2.2. $LiNbO_3$ waveguide

For the slab waveguide, the same effect of decreasing amplitude of the electric field generated by

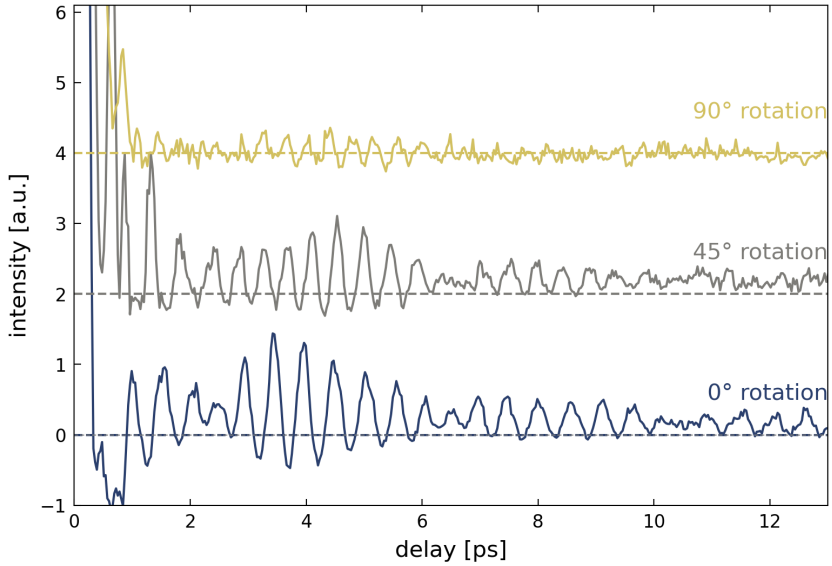

(a) Time resolved data for different rotation angles of the sample in waveguide $LiNbO_3$

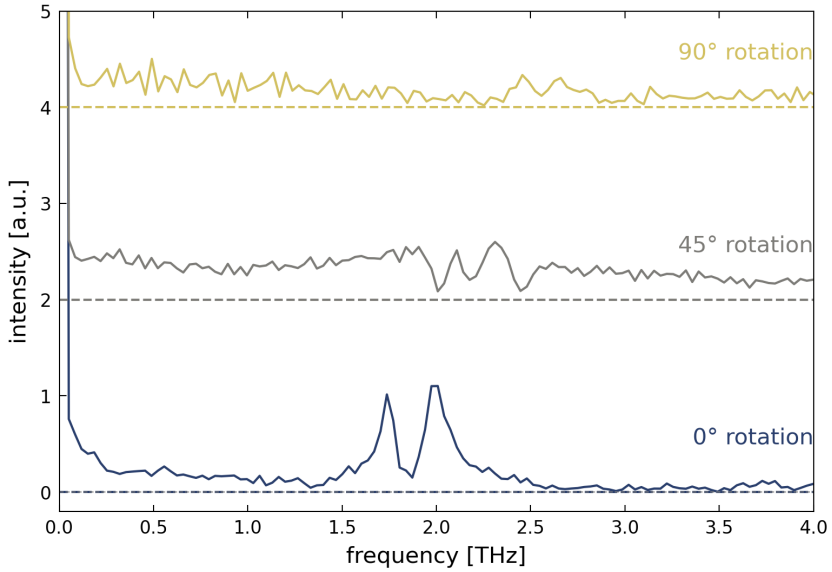

(b) Fourier analysis of the data from t=0.6 ps to 13 ps at different rotation angles of the sample in a $LiNbO_3$ waveguide

Figure 3.9.: Time resolved data and Fourier analysis for different rotation angles of the sample in waveguide $LiNbO_3$. The wavelength of the transient grating is $\lambda_{tg} = 26.2\,\mu$m, the fluence yields 86 mJ/(cm)^2

the phonon-polaritons with increased rotation angle due to varying polarizability is evident in fig.3.8(a). In contrast to the bulk, even for an angle of 90 degrees, a small oscillation of the intensity is apparent. Since in literature the polarizability is approximated for bulk samples there might be a slight difference regarding the absolute values for the slab waveguide and bulk [41] resulting in a weaker decrease of the oscillation amplitude of the electric field generated by phonon-polaritons for waveguide modes than for bulk. Additionally, as mentioned above, the damping of phonon-polaritons that are excited in the $LiNbO_3$ waveguide, may undergo a weaker damping since a large contribution of the evanescent THz field propagates outside the waveguide.
The Fourier analysis in fig.3.9(b) for 0° rotation exhibits two peaks of the intensity at different frequencies, i.e. two excited modes inside the waveguide, that shift with increasing rotation angle due to a mixture of TE and TM modes. Such effects are described in the paper by Yang et al.[10] but not discussed here, where I only study the behavior of TM modes. In theory, three modes should be excited by using a phase mask pattern with a wavelength of $\lambda_{PM} = 38.3\mu$m, but only two are observed in this experiment.
In general, oscillations with frequencies that approach a resonance frequency experience large damping rates since the imaginary part of the dielectric function, respectively refractive index, peaks at resonance frequencies (cf. fig.1.9). The frequency-dependent damping rate γ_{PP} of a phonon-polaritons yields

$$\gamma_{PP} = \omega_{PP} \frac{\Im\mathfrak{m}(n(\omega_{PP}))}{\Re\mathfrak{e}(n(\omega_{PP}))} = v_{Ph} \cdot \Im\mathfrak{m}(n(\omega_{PP})). \tag{3.5}$$

In the waveguide another effect occurs due to the distribution of the electric field of phonon-polaritons in the anisotropic waveguide, more extensively discussed in the next section.
Hence, the signal of the oscillations in the intensity pattern of the second mode (m=2) is attenuated by damping effects and thus the second mode is not visible in the signal. In [10] this behavior occurs as well for the second transverse magnetic mode for similar wave vectors.

3.3. Displacement series in bulk and waveguide

The following section employs the propagation behavior of low frequency phonon-polariton wave packets providing low damping rates according to equation 3.5 and fig.1.10a). The low energy phonon-polaritons possesses light-like behavior and properties[†] like reflection [43], diffraction effects [44], guidance behavior [45], interference[6] or propagation through material for several millimeters can be observed better [46], [10].
The propagation of phonon-polariton wave packets is discussed in detail in the following section for both samples, the bulk and a slab waveguide containing a thickness of 50 μm. By displacing the probe beam with respect to the pump beam up to roughly 1.5 mm in five steps, the time resolved data and their Fourier analysis for different displacements are provided. The combination of low damping rates for the resulting wave vector for this phase mask pattern and the feasible block of one of the probe beam, respectively $\mathbf{k}_3$, leads to the choice of using a phase mask pattern of λ_{PM}=114.8 μm for both samples. For larger phase mask patterns the probe beams are insufficient separated spatially. Blocking the probe beam entirely was not provided for those. The displacement of the probe beam relative to the pump beam is measured by analyzing the images of the CCD-camera, which are included in the appendix C for the two representative displacements of 0 μm and 1550 μm.

[†]Some of these properties also occur for high energy phonon-polaritons which are not discussed furthermore.

3.3.1. $LiNbO_3$ bulk

Since the signal amplitude in fig.3.4 is maximized for fluences between 40 and 100 mJ/(cm)^2, the propagation was investigated with a fluence of 98 mJ/(cm)^2 for the pump and 7 mJ/(cm)^2 corresponding to the probe beam. In fig.3.10 the time resolved data for different displacements of the probe beam compared to the pump beam is presented. From this figure, the temporal center

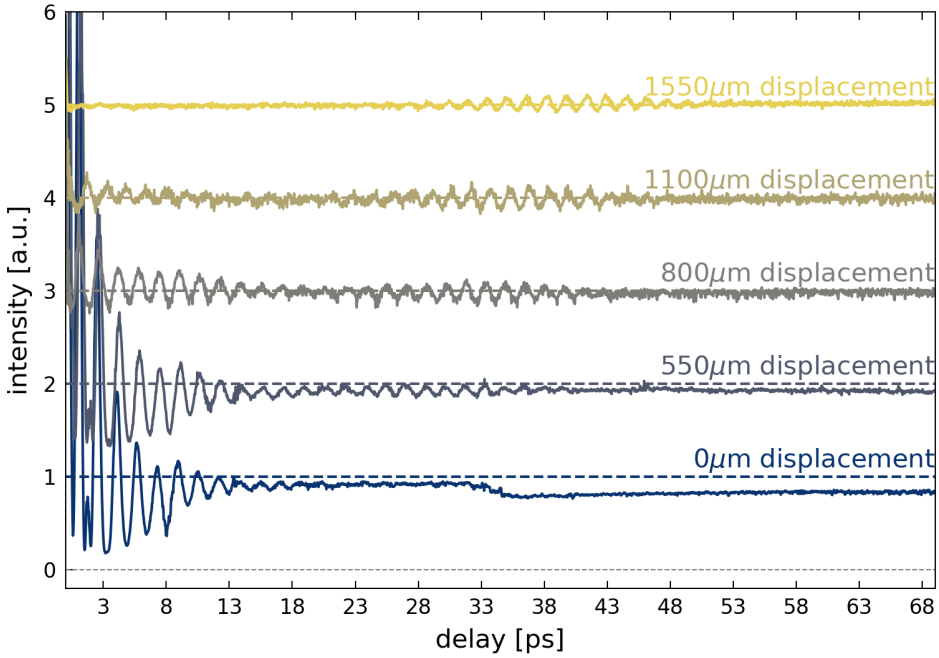

Figure 3.10.: Time resolved data for different displacements of the probe and pump beam in bulk $LiNbO_3$. The dip of the graph corresponding to 0 μm displacement at 35 ps dedicates an instability of the laser.

of the wave packets may be selected by determining the delay time associated with the highest amplitude of oscillation of the intensity. It is evident that for slightly displaced probe and pump beams (0-1100 μm) the intensity at 0ps reaches its maximum. If a Fourier analysis over a temporal range of 10 ps is implemented the range providing the highest amplitude at the phonon-polariton frequency, only for 1100 μm and 1550 μm reasonable central delay times are calculated. Thus, only for the displacement of 1550 μm the group velocity v_g and group index n_{group} is examined explicitly. The central delay time thus propagation time yields $\tau = 40.1$ ps, by my own experience I estimate the uncertainty of the displacement to be 50 μm based on a not perfect overlap of both pump pulses. The uncertainty of the delay time is estimated to 1ps due to the vague determination of the highest amplitude of oscillation of the intensity. The propagation distance of the phonon-polariton wave packet requires considering the propagation direction of phonon-polaritons in $LiNbO_3$ discussed in section 1.2.2. The wave packet propagates into the depth of the sample by Δs, which is the identified with the actual propagation distance, determined by the angle β that is defined as shown in fig.1.1c). The wave vector of the transient grating is calculated in the appendix C.

$$\beta = \arccos\frac{k_{tg}}{q} = 19.7^\circ \Rightarrow \Delta s = \frac{\Delta d}{\cos\beta} = 1700\,\mu\text{m}$$

The group velocity and refractive index yields

$$v_g = \frac{\Delta s}{\tau} = 4.24 \cdot 10^7 \frac{m}{s} \Rightarrow n_{\text{group}} = 7.07 \pm 0.35$$

The literature value of $n_{group,lit}$=6.8 is in agreement with the observation and within the calculated uncertainty [30].
The Fourier analysis over the entire temporal range of time resolved data shown in fig.3.11 exhibits the disappearance of the second peak of the frequency that was already discussed in section 3.1. The decrease of the second maximum occurs because the amplitude of the electric field generated by the phonon-polaritons is damped with time, i.e. with the distance of propagation. The rate of probe beam diffraction at impurities remains nearly constant, thus $E^{ela} \gg E^{\pm}$ approximates the behavior of the graph for larger displacements.

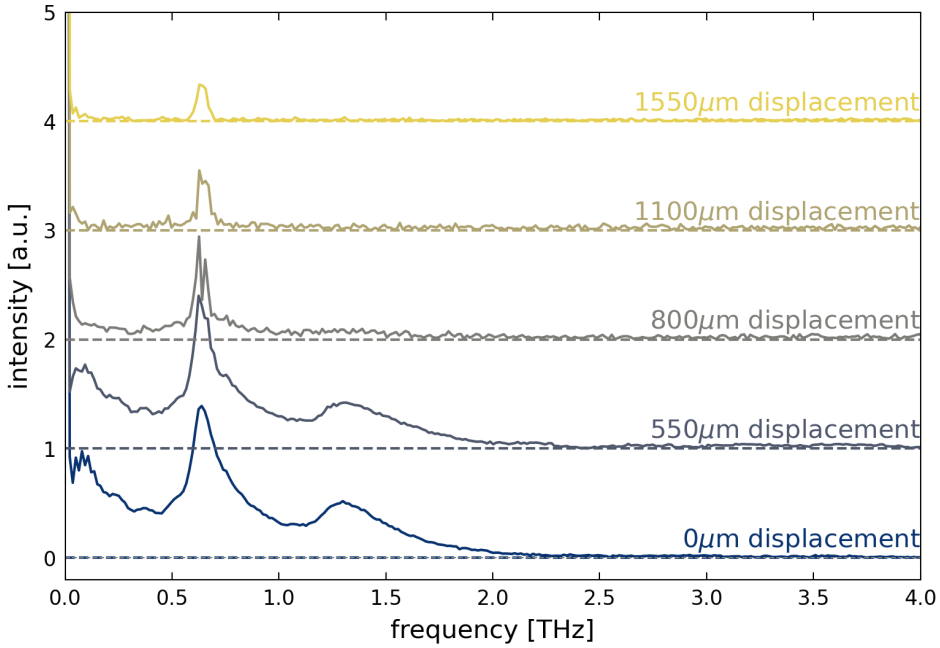

Figure 3.11.: Fourier analysis of the time resolved data from 0.6 ps to 70 ps for different displacements of the probe and pump beam in bulk $LiNbO_3$.

3.3.2. $LiNbO_3$ waveguide

The same fluences and phase mask pattern parameters from the bulk apply for the waveguide measurement to allow for direct comparison between the displacement series experiments in the $LiNbO_3$ bulk and waveguide.
The time resolved data for the waveguide displacement series is depicted in fig.3.12. Similar to the fluence series at the waveguide previously, three transverse magnetic waveguide modes are excited at perfect overlap of the pump and probe beam, i.e. 0 μm displacement. The decrease of the peaks in the Fourier analysis in fig.3.13 of the first and second mode is explained by fig.1.16c), a large fraction of the electric field is located outside the waveguide and this fraction is estimated to experience less damping as it propagates in free space. It is apparent, that the amount of the field outside decreases with rising mode number m. Thus, the higher modes are more strongly damped than the zeroth mode. The peak of the zeroth waveguide mode in the Fourier analysis persists for long displacements, hence long delay times.
To derive the group velocity and thus the group index of the three transverse magnetic waveguide-modes excited in this experiment similarly to the bulk only the calculation is derived for a displacement Δd = 1550 μm since for the waveguide the propagation direction of the phonon-polaritons is approximated to be perpendicular to the surface of the sample and parallel to the wave vector of the

transient grating due to the confined thickness of the waveguide.

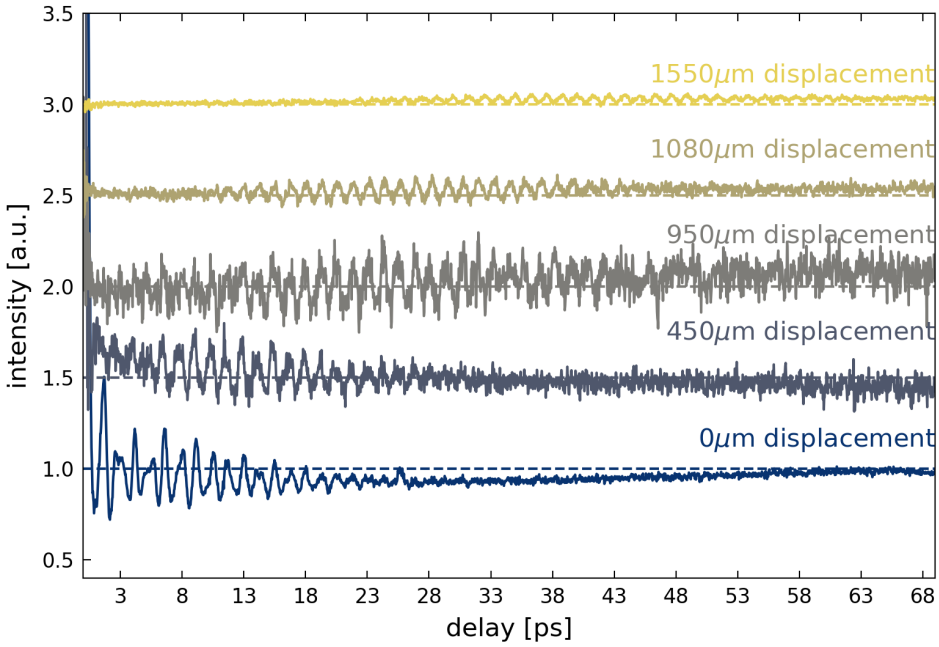

Figure 3.12.: Time resolved data for different displacements of the probe and pump beam in slab waveguide $LiNbO_3$.

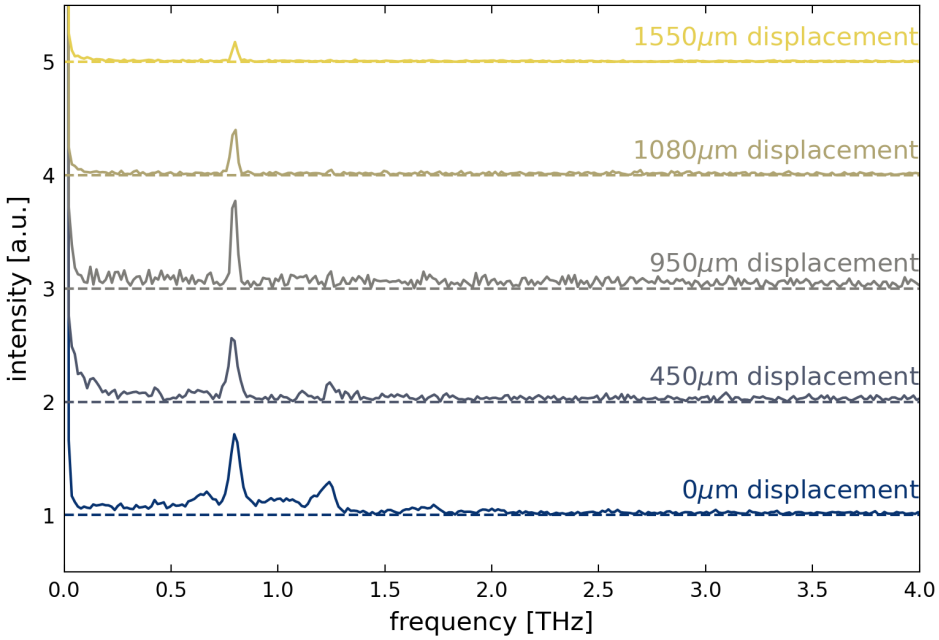

Figure 3.13.: Fourier analysis of the time resolved data from 0.6 ps to 70 ps for different displacements of the probe and pump beam in a slab waveguide $LiNbO_3$

Since the first and second excited TM mode are damped significantly apart from 450 μm, only the

zeroth mode is analyzed. Its delay times states $\tau = 40.5$ ps.

$$v_g = \frac{\Delta d}{\tau} = 3.83 \cdot 10^7 \frac{m}{s} \Rightarrow n_{\text{group}} = 7.83 \pm 0.39$$

The calculated value of $n_{group,sim}$=8.14 extracted from fig.1.16a) lies within the estimated uncertainty range of the experimentally obtained result.

3.4. Comparison with the dispersion relations

To conclude the previous measurements, the data is compared to the dispersion relations of the slab waveguide and of bulk $LiNbO_3$, that have been derived previously in chapter 1. Fig.3.14 shows the comparison between the experimental data and the theoretical results. The calculated wave vector of the transient grating k_{tg} is derived in the appendix for every measurement series, in Appendix C. A summary of the calculated and measured data is given in tab.A.1 in the appendix.

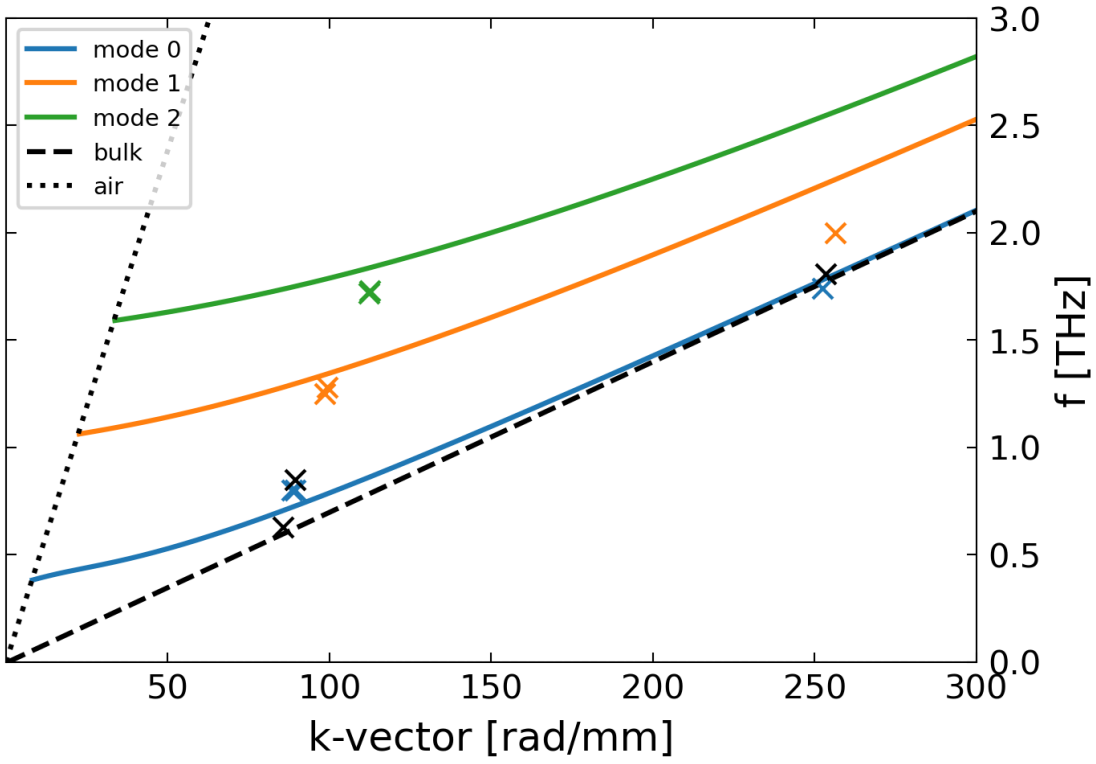

Figure 3.14.: Dispersion relation of the first three excited TM modes in the waveguide and the bulk, both consisting of $LiNbO_3$ x-cut. The waveguide branches are shown in color, whereas the bulk is depicted as a black dashed line. Crosses mark the peaks of the Fourier spectrum in the experimentally observed spectra from the data presented in this thesis

The measured data are in reasonable agreement with the theoretical calculation of the dispersion relations. A determination of the uncertainty is omitted due to the manifold experimental contributions that are difficult to disentangle at this stage.

4. Conclusion and outlook

This thesis covers the transient grating excitation of phonon-polaritons in an anisotropic waveguide in comparison to a bulk specimen of lithium niobate. The propagation, damping behavior, detection and dispersion relations of phonon-polaritons in the slab waveguide are examined and compared to the bulk, that was investigated by previous work in the group [21].
In the thin waveguide sample of 50 μm thickness, several transverse magnetic modes are excited. Their origin and dispersion branches are derived theoretically, and their presence has been confirmed experimentally [34].
The experimental setup using a transient grating of this pump-probe experiment makes use of the box-CARS arrangement, where three spatially separated beams overlap at the sample spot to selectively excite phonon-polaritons with a tunable wave vector that is determined the angle of intersection between the two pump-beams. In the first part of this thesis, the fluence dependence of the pump beam on the detection signal of the phonon-polaritons is investigated. Homodyne detection effects in three different limiting cases of the magnitude of the electric field parts incident at the spectrometer explain the occurrence of a second peak in the Fourier analysis at twice the actual frequency of the phonon-polaritons. The exact origin of the elastic scattering contribution that limits $E^{ela} \gg E^{\pm}$ is narrowed down to two possibilities, a residual electric field incident at the spectrometer from the not perfectly blocked probe beam $\mathbf{k}_3$ or scattering at impurities and the surface of the sample of the excitation beams $\mathbf{k}_1$ and $\mathbf{k}_2$ or the probe beam $\mathbf{k}_4$. In a future study a neutral density filter may be used instead of a block as already done in [20] to control the intensity of the attenuated reference beam. A limiting factor in the experimental work was the difficulty of completely blocking the reference probe beam (k_3) and no parts of the other beams, especially at for large wavelengths of the phase mask pattern. For the waveguide, the second peak in the Fourier spectrum does not occur, but three modes are excited as predicted previously.
Afterwards, another phase mask pattern with a smaller wavelength is used and the rotation angle of the c-axis regarding the wave vector of the transient grating alters in 45° steps. In this experiment the importance of a well-oriented sample is shown for the bulk and waveguide likewise. The signal vanishes for the bulk entirely at a rotation angle of 90° between the c-axis and the wave vector of the transient grating, i.e. when the c-axis is oriented perpendicular to the polarization of the excitation beams. In contrast, for the waveguide, the peaks in the Fourier analysis decrease in their magnitude and are blue shifted with increasing rotation angle. A possible explanation is the simultaneous excitation of transverse electric and magnetic modes, which was already observed in [10], where the c-axis and the polarization of the beam remain parallel, but the wave vector of the transient grating is rotated within the plane of the sample. Since this is a different experimental approach than in this thesis, it requires an additional theoretical model to describe the blue shift, which is not provided in this work.
In the third part, the propagation of phonon-polaritons is examined with displacements of the pump beams up to 1.5 mm with respect to the probe beam. The distance between both beams is determined with an analysis of the beam profiles on a camera at the sample position, and the delay time is extracted from the presented time resolved data of the phonon-polaritons oscillations. For the bulk sample of $LiNbO_3$ a group index of $n_{group} = 7.07 \pm 0.35$ is calculated. In the anisotropic slab waveguide the first and second mode disappear at large displacements due to their higher damping rates compared to the zeroth mode. This damping occurs because a larger fraction of the electric field of the phonon-polaritons located inside the waveguide for increasing mode number. The group

index of the first excited mode, thus the zeroth waveguide mode states $n_{group} = 7.83 \pm 0.39$, slightly underestimates the theoretical value.
The work by Yang et al. [10] studies the excitation of transverse electric and transverse magnetic modes in a similar slab waveguide and compares the energy stored in the electric field of different modes. They find that TE modes are excited more efficiently than TM modes when a similar excitation fluence is used. Thus, future studies could investigate the propagation of TE modes and extend the displacement series and observe reflections at the edge of the sample. In this work, a displacement distance of roughly 2000 μm did not provide any visible signature of phonon-polaritons in the time resolved data for TM modes.
The frequencies and wave vectors of the excited phonon-polaritons are extracted from the measured data and plotted with the simulated dispersion relation of the bulk and waveguide of $LiNbO_3$. With an increased magnitude of the signal and further propagation of the wave packets, a thin antiferromagnetic sample, e.g. erbium orthoferrite $ErFeO_3$ could be placed onto the bulk sample of $LiNbO_3$ and magnon-phonon-polariton modes may be induced and investigated as previously demonstrated by Sivarajah et al. [47]. Generally, this allows selective excitation of samples in close proximity to the waveguide with well-defined THz frequency.
To examine the entire dispersion relation the experimental setup phase masks with different wave vectors are needed. By sending the pump beam directly onto the sample without the use of a phase mask, multiple phonon-polaritons with different wave vectors would be excited at the same time. The dispersion relation may then be extracted from Fourier analyzing space-time images as done by Feurer et al. or Yang et al. [6], [10].

A. Appendix

A. Derivation of the group velocity

The calculation of the group velocity of different phonon-polariton branches in waveguides follows the steps present in the book of Cronin[34], pages 73-76, adapted to transverse magnetic modes. Starting from the eigenvalue equation 1.22 and the trigonometric relation $k_z = n_1 k_0 \sin\Theta_i$, differentiating with respect to k_z yields

$$\frac{\mathrm{d}}{\mathrm{d}k_z}\left[k_{1x}d - \frac{m\pi}{2}\right] = \frac{\mathrm{d}}{\mathrm{d}k_z}[\Phi]$$

$$\frac{d\cdot\cos\Theta_i}{c}\left(n_1 + \omega\frac{\mathrm{d}n_1}{\mathrm{d}\omega}\right)\frac{\mathrm{d}\omega}{\mathrm{d}k_z} - k_0 n_1 d\sin\Theta_i\frac{\mathrm{d}\Theta_i}{\mathrm{d}k_z} - \frac{\mathrm{d}\Phi}{\mathrm{d}k_z} = 0 \tag{A.1}$$

and

$$\frac{\mathrm{d}}{\mathrm{d}k_z}k_z = \frac{\mathrm{d}}{\mathrm{d}k_z}[n_1 k_0\sin\Theta_i] \tag{A.2}$$

$$1 = \frac{\sin\Theta_i}{c}\left[n_1 + \omega\frac{\mathrm{d}n_1}{\mathrm{d}\omega}\right]\frac{\mathrm{d}\omega}{\mathrm{d}k_z} + k_0 n_1\cos\Theta_i\frac{\mathrm{d}\Theta_i}{\mathrm{d}k_z}. \tag{A.3}$$

Since the dispersion relation in fig.1.10b) may be approximated linearly for small wave vectors, material dispersion $\mathrm{d}n_1/\mathrm{d}\omega$ is neglected. I can extract $\mathrm{d}\Theta_i/\mathrm{d}k_z$ by rearranging equation A.1. Insert that in equation A.3 yields the group velocity v_g as:

$$v_g = \frac{\mathrm{d}\omega}{\mathrm{d}k_z} = \frac{d\tan\Theta_i + \frac{\partial\Phi}{\partial k_z}}{\frac{dn_1}{c\cos\Theta_i} - \frac{\partial\Phi}{\partial\omega}},$$

wherein I use the expansion of the total differential $\frac{\mathrm{d}\Phi}{\mathrm{d}k_z} = \frac{\partial\Phi}{\partial k_z} + \frac{\partial\Phi}{\partial\omega}\cdot\frac{\partial\omega}{\partial k_z}$. Differentiating the expression for Φ in equation 1.18 results in:

$$\frac{\mathrm{d}}{\mathrm{d}k_z}\tan\Phi = \frac{\mathrm{d}}{\mathrm{d}k_z}\frac{\gamma n_1^2}{k_{1x}n_2^2}$$

$$\Leftrightarrow (1+\tan^2\Phi)\frac{\partial\Phi}{\partial k_z} = \frac{n_1^2}{n_2^2}\cdot\left[\frac{k_{1x}\frac{\partial\gamma}{\partial k_z} - \gamma\frac{\partial k_{1x}}{\partial k_z}}{k_{1x}^2}\right].$$

The Pythagorean theorem in $\gamma = \sqrt{(n_2^2 - n_1^2\sin^2(\Theta_i))k_0^2}$ yields the derivatives:

$$\frac{\partial k_{1x}}{\partial k_z} = -\frac{k_z}{k_{1x}} \text{ and } \frac{\partial\gamma}{\partial k_z} = \frac{k_z}{\gamma}.$$

With these expressions and again equation 1.22 the final result emerges

$$\frac{\partial\Phi}{\partial k_z} = \frac{n_1^2 n_2^2\left[k_z k_{1x}^2 + \gamma^2 k_z\right]}{k_{1x}^3\gamma n_2^4 + \gamma^3 k_{1x} n_1^4}.$$

For the derivation with respect to ω the same procedure and $k_0 = \omega / c$ is applied

$$\frac{\partial \Phi}{\partial \omega} = -\frac{n_1^2 n_2^2 \left[k_{1x}^2 \omega n_2^2 + \gamma^2 n_1^2 \omega\right]}{c^2 \left(k_{1x}^3 \gamma n_2^4 + \gamma^3 k_{1x} n_1^4\right)}.$$

Both expressions are slightly more complex than the corresponding equations for the TE modes:

$$\frac{\partial \Phi}{\partial k_z} = \frac{k_z (k_{1x}^2 + \gamma^2)}{k_{1x} \gamma (n_1^2 - n_2^2) k_0^2}$$
$$\frac{\partial \Phi}{\partial \omega} = -\frac{k_{1x}^2 n_2^2 + \gamma^2 n_1^2}{\omega (n_1^2 - n_2^2) \gamma k_{1x}}.$$

Both, transverse electric and magnetic modes and their coupling is extensively discussed in [10]. A comparison of their dispersion relation is depicted in fig.A.1

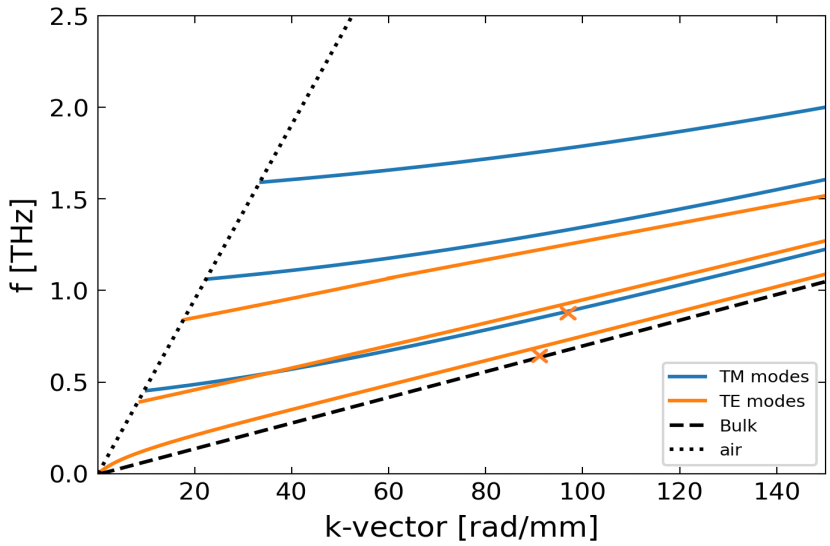

Figure A.1.: Comparison of the dispersion relation of transverse electric (TE) and transverse magnetic (TM) waveguide modes.

B. Calculation of the intersection angle Θ_{air}

To derive the wave vector of the phonon-polaritons, the intersection angle of the beams on the sample and the wavelength of the transient grating are required, to confer equation 1.5, both variables are calculated in the following two sections and summarized in section D. The condition for an optical grating or transmission grating yields for the first order

$$\lambda_{exc} = \sin \frac{\Theta'_{air}}{2} \lambda_{PM}$$
$$\Rightarrow \frac{\Theta'_{air}}{2} = \arcsin\left(\frac{\lambda_{exc}}{\lambda_{PM}}\right) \tag{B.4}$$

Trigonometry applied on the left triangle between the phase mask, cylindrical lens and the separated beams provides

$$\tan \frac{\Theta'_{air}}{2} = \frac{\Delta x}{f_1}$$
$$\Rightarrow \Delta x = f_1 \tan \frac{\Theta'_{air}}{2} \tag{B.5}$$

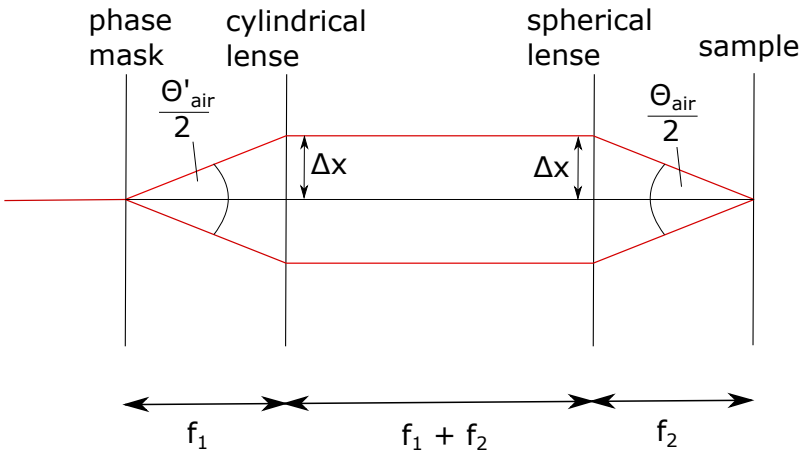

Figure A.2.: Simplified sketch of the lens-system that is used to image the phase mask as intensity patter non the sample. (View from top)

Similar the right triangle by substituting equation B.5

$$\begin{aligned}\tan\frac{\Theta_{\text{air}}}{2} &= \frac{\Delta x}{f_2}\\ &= \frac{f_1}{f_2}\tan\frac{\Theta'_{\text{air}}}{2}\end{aligned}$$

Inserting into equation B.4 yields

$$\frac{\Theta_{\text{air}}}{2} = \arctan\left[\frac{f_1}{f_2}\tan\left(\arcsin\frac{\lambda_{\text{exc}}}{\lambda_{\text{PM}}}\right)\right] \tag{B.6}$$

(B.7)

In the setup shown in chapter 2 the focal lengths are set to f_1 = 75 mm and f_2 = 100 mm, the central wavelength of the excitation light is approximately λ_{exc} = 807 nm and the most frequently used phase mask pattern in this thesis has a period of 120 μm so the intersection angle Θ_{air} can be calculated to be:

$$\Theta_{\text{air}} = 0.58^\circ = 0.01\text{rad} \tag{B.8}$$

Thus the small-angle approximation is well satisfied and equation B.6 simplifies to:

$$\frac{\Theta_{\text{air}}}{2} = \arctan\left[\frac{f_1}{f_2}\left(\frac{\lambda_{\text{exc}}}{\lambda_{\text{PM}}}\right)\right].$$

C. Calculation of the wavelength of the transient grating

Here, I shortly explain the transient grating excitation and analysis of the beam profiles. The real space imaging of the intensity of the intersecting pump beams, or incident probe beam is depicted in the lower left pattern, the pixel size of the CCD detector of 1.85 μm x 1.85 μm is used for conversion to length. At the maximum of the x and y component a horizontal, respectively vertical cut is made and the FWHM for each cut is determined by fitting a Gaussian envelope function. Additionally, a Fourier analysis of the horizontal cut is provided in order to determine the spatial period of the transient grating excitation.

Fluence series

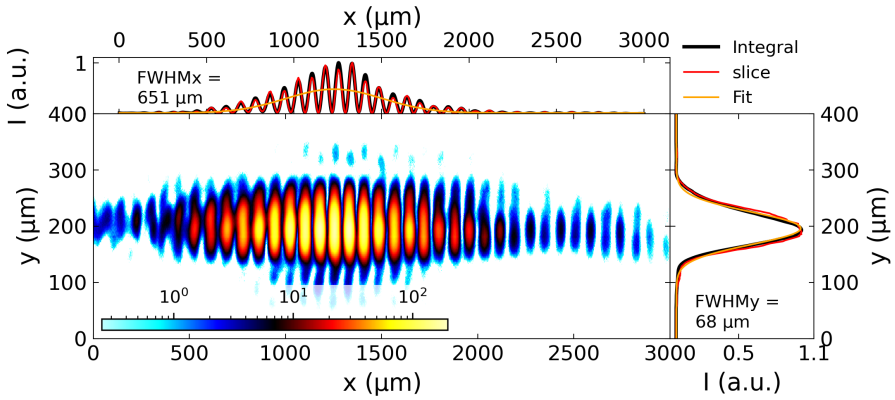

(a) Beam profile of the pump beam for the fluence series

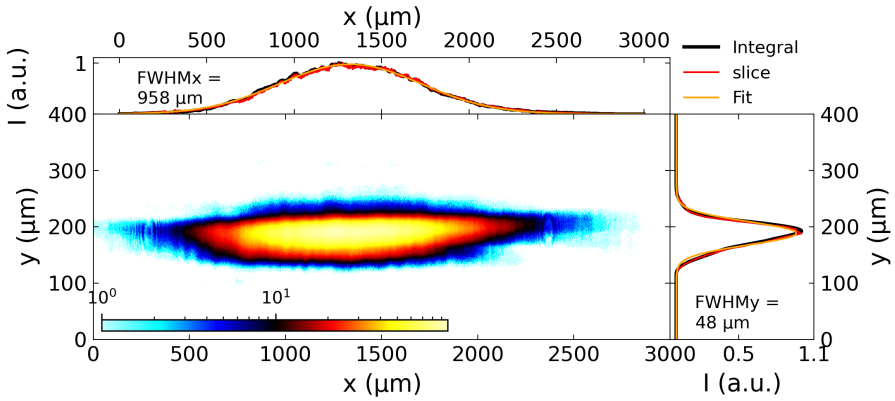

(b) Beam profile of the probe beam for the fluence series

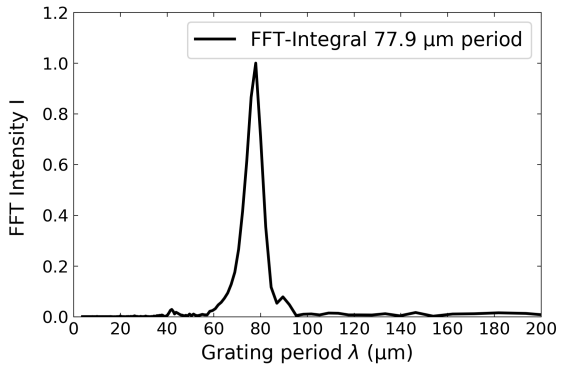

(c) Fourier analysis of the pump beam profile for fluence series

Figure A.3.: Beam profiles for the pump beam depicted in a) and probe beam, shown in b) and the Fourier analysis of the pump beam in c) for the fluence series experiments.

The transient grating wave vector k_{tg} of the fluence series yields

$$\lambda_{tg} = 77.9 \mu m$$
$$\Rightarrow k_{tg} = 80.6 \frac{\text{rad}}{\text{mm}}$$

Rotation series

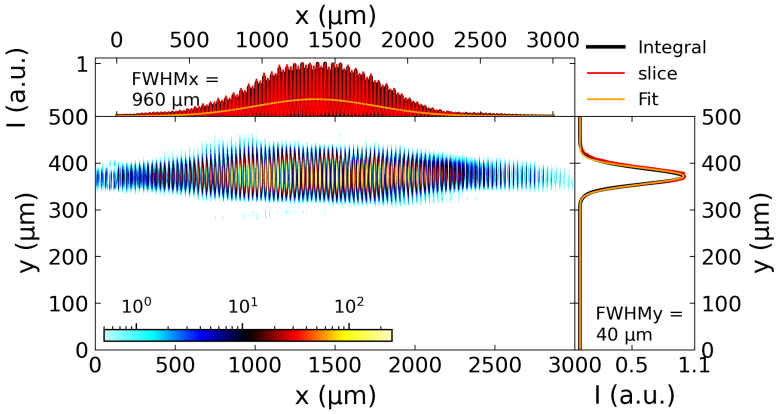

(a) Beam profile of the pump beam for the rotation series

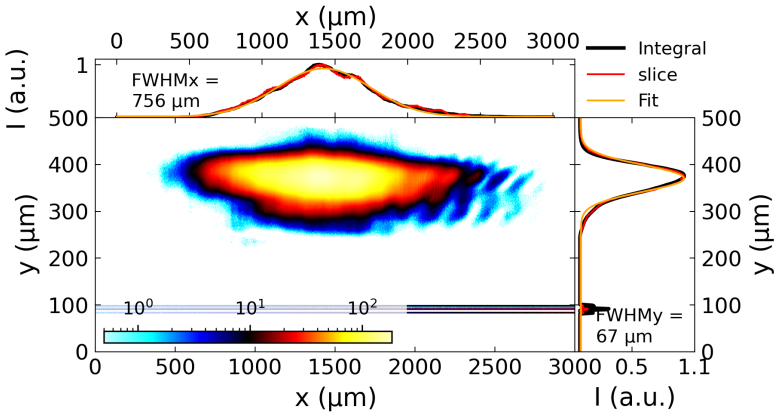

(b) Beam profile of the probe beam for the rotation series

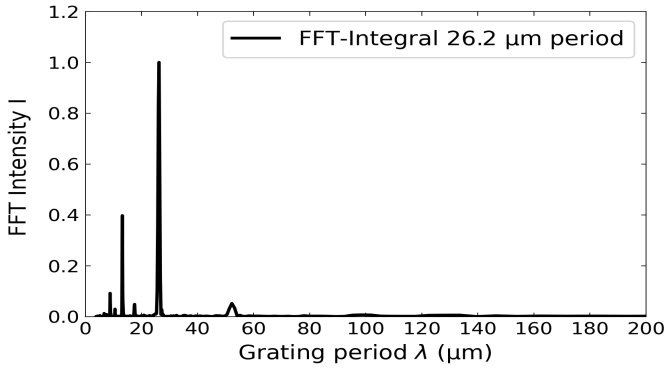

(c) Fourier analysis of the pump beam profile for rotation series

Figure A.4.: Beam profiles for the pump beam depicted in a) and probe beam, shown in b) and the Fourier analysis of the pump beam in c) for the rotation series experiments.

The transient grating wave vector k_{tg} of the rotation series yields

$$\lambda_{tg} = 26.2\,\mu\text{m}$$

$$\Rightarrow k_{tg} = 240.0\frac{\text{rad}}{\text{mm}}$$

Displacement series

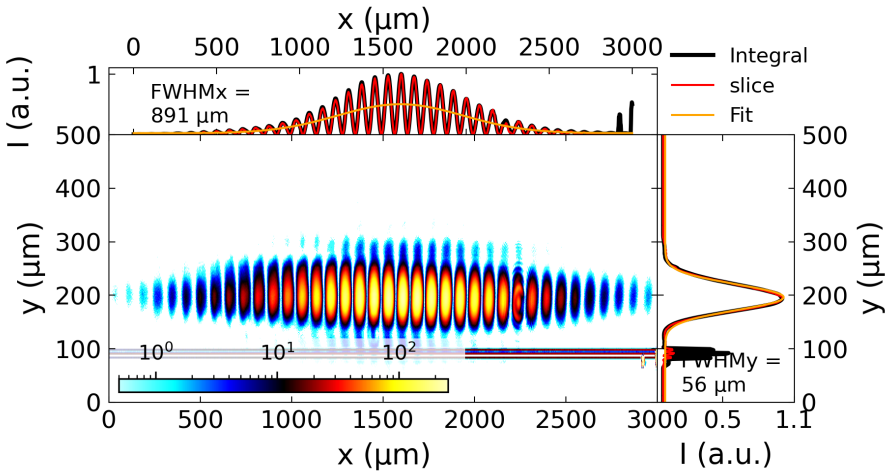

(a) Beam profile of the pump beam for the 0μm displacement

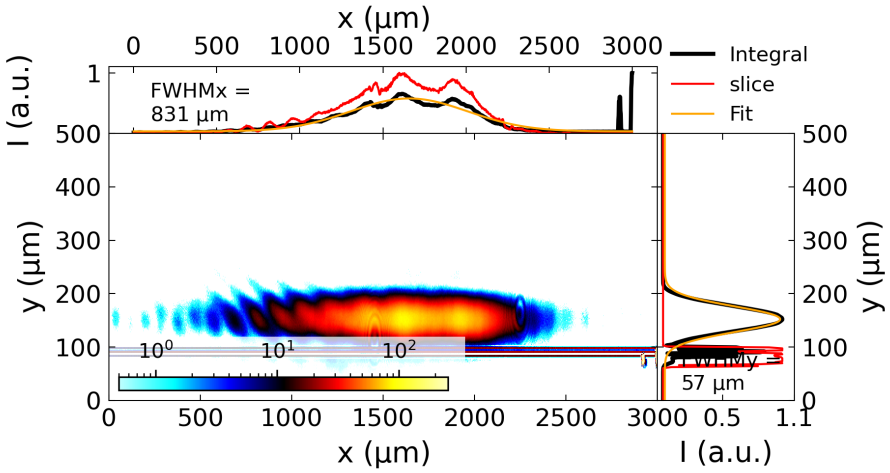

(b) Beam profile of the probe beam for the 0μm displacement

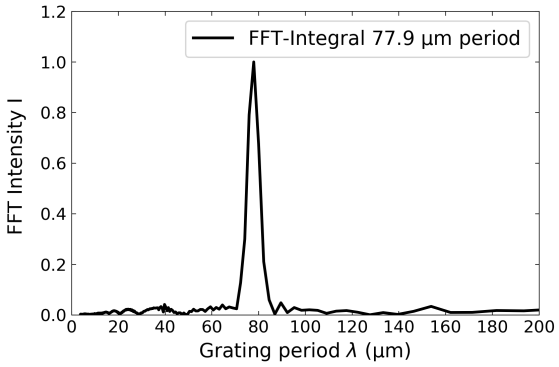

(c) Fourier analysis of the pump beam profile for 0 μm

Figure A.5.: Beam profiles for the pump beam depicted in a) and probe beam, shown in b) and the Fourier analysis of the pump beam in c) for the displacement series experiments at a displacement of 0 μm.

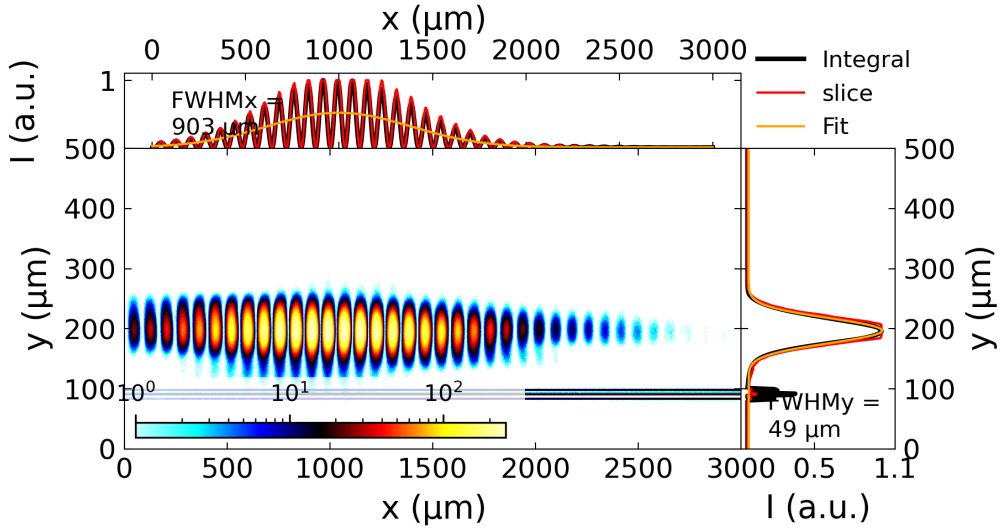

(a) Beam profile of the pump beam for the 1550 μm displacement. The observed x-range is shifted by 1550 μm compared to the probe beam, thus the displacement amounts to 1550 μm and the resolution remains sufficient

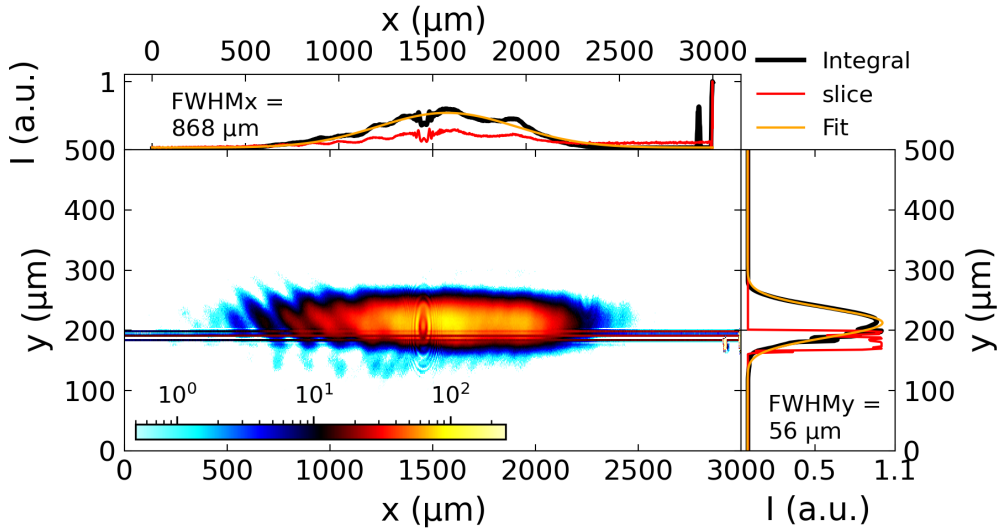

(b) Beam profile of the probe beam for the 1550 μm displacement.

Figure A.6.: Beam profiles for the pump beam depicted in a) and probe beam, shown in b) for the displacement series experiments.

The transient grating wave vector k_{tg} of the displacement series yields

$$\lambda_{tg} = 77.9 \mu m$$
$$\Rightarrow k_{tg} = 80.6 \frac{\text{rad}}{\text{mm}}$$

D. Summary of the measured and calculated data

The derivation of the wave vector of the phonon-polaritons q is given in equation 1.5. Every series is separated into the two examined samples, the bulk and waveguide (wg). For the waveguide data, I distinguish between the three excited modes (0^{th}, 1^{st} and 2^{nd}.)

Table A.1.: Summary of the measured and calculated data

series	sample	λ_{PM} [μm]	λ_{tg}[μm]	k_{tg}[rad/mm]	Θ_{air}[$^\circ$]	q[rad/mm]	f_{PP}[THz]
fluence	bulk	114.8	77.9	80.6	0.60	89.4	0.85
fluence	wg 0^{th}	114.8	77.9	80.6	0.60	88.4	0.80
fluence	wg 1^{st}	114.8	77.9	80.6	0.60	99.4	1.28
fluence	wg 2^{nd}	114.8	77.9	80.6	0.60	112.2	1.72
rotation	bulk	38.3	26.2	240.0	2.65	253.3	1.80
rotation	wg 0^{th}	38.3	26.2	240.0	2.65	252.5	1.74
rotation	wg 1^{st}	38.3	26.2	240.0	2.65	256.2	1.99
displacement	bulk	114.8	77.9	80.6	0.60	85.6	0.63
displacement	wg 0^{th}	114.8	77.9	80.6	0.60	88.2	0.80
displacement	wg 1^{st}	114.8	77.9	80.6	0.60	98.6	1.25
displacement	wg 2^{nd}	114.8	77.9	80.6	0.60	112.4	1.73

Bibliography

[1] Y.-S. Lee, T. Meade, V. Perlin, H. Winful, T. B. Norris, and A. Galvanauskas, "Generation of narrow-band terahertz radiation via optical rectification of femtosecond pulses in periodically poled lithium niobate," Applied Physics Letters **76**, 2505–2507 (2000).

[2] C. Schmuttenmaer, "Exploring dynamics in the far-infrared with terahertz spectroscopy.," Chemical reviews **104 4**, 1759–79 (2004).

[3] B. Ferguson and X.-C. Zhang, "Materials for terahertz science and technology," Nature Materials **1**, 26–33 (2002).

[4] M. C. Hoffmann and J. A. Fülöp, "Intense ultrashort terahertz pulses: generation and applications," Journal of Physics D: Applied Physics **44**, 083001 (2011).

[5] R. Loudon, "The Raman effect in crystals," Advances in Physics **13**, 423–482 (1964).

[6] T. Feurer, N. S. Stoyanov, D. W. Ward, J. C. Vaughan, E. R. Statz, and K. A. Nelson, "Terahertz Polaritonics," Annual Review of Materials Research **37**, 317–350 (2007).

[7] K. A. Nelson, R. J. D. Miller, D. R. Lutz, and M. D. Fayer, "Optical generation of tunable ultrasonic waves," Journal of Applied Physics **53**, 1144–1149 (1982).

[8] M. Sander, M. Herzog, J. E. Pudell, M. Bargheer, N. Weinkauf, M. Pedersen, G. Newby, J. Sellmann, J. Schwarzkopf, V. Besse, V. V. Temnov, and P. Gaal, "Spatiotemporal Coherent Control of Thermal Excitations in Solids," Phys. Rev. Lett. **119**, 075901 (2017).

[9] R. A. Duncan, F. Hofmann, A. Vega-Flick, J. K. Eliason, A. A. Maznev, A. G. Every, and K. A. Nelson, "Increase in elastic anisotropy of single crystal tungsten upon He-ion implantation measured with laser-generated surface acoustic waves," Applied Physics Letters **109**, 151906 (2016).

[10] C. Yang, Q. Wu, J. Xu, K. A. Nelson, and C. A. Werley, "Experimental and theoretical analysis of THz-frequency, direction-dependent, phonon polariton modes in a subwavelength, anisotropic slab waveguide," Opt. Express **18**, 26351–26364 (2010).

[11] Z. Chen, "Modeling phonon-polariton generation and control in ferroelectric crystals," PhD dissertation (Massachusetts Institute of Technology, 2009).

[12] K. Huang, "Lattice Vibrations and Optical Waves in Ionic Crystals," Nature **167**, 779–780 (1951).

[13] Y. R. Shen and N. Bloembergen, "Theory of Stimulated Brillouin and Raman Scattering," Phys. Rev. **137**, A1787–A1805 (1965).

[14] R. Gross and A. Marx, Festkörperphysik (De Gruyter Oldenbourg, 2014).

[15] C. Kittel, "Einführung in die Festkörperphysik, 3. erweiterte und verbesserte Auflage, München-Wien. R. Oldenbourg Verlag. 1973. 877 S., 519 Abb., 59 Tabellen .," **57**, https://doi.org/10.1002/zamm.19770570220 (1977).

[16] T. Mitsui, "Ferroelectrics and Antiferroelectrics," in Springer Handbook of Condensed Matter, edited by W. Martienssen and H. Warlimont (Springer Berlin Heidelberg, Berlin, Heidelberg, 2005), pp. 903–938.

[17] A. von Hoegen, "Probing Nonlinear Dynamics in Strongly Driven Quantum Materials," PhD dissertation (Universität Hamburg, 2021).

[18] C. J. Brennan, "Femtosecond wavevector overtone spectroscopy of anharmonic lattice dynamics in ferroelectric crystals," PhD dissertation (Massachusetts Institute of Technology, 1997).

[19] Y.-X. Yan and K. A. Nelson, "Impulsive stimulated Raman, Brillouin, and Rayleigh scattering - Comprehensive theory and comparison between time-domain and frequency-domain light scattering spectroscopies," in Lasers '86; Proceedings of the Ninth International Conference on Lasers and Applications (Jan. 1987), pp. 62–66.

[20] T. F. Crimmins, N. S. Stoyanov, and K. A. Nelson, "Heterodyned impulsive stimulated Raman scattering of phonon–polaritons in $LiTaO_3$ and $LiNbO_3$," The Journal of Chemical Physics **117**, 2882–2896 (2002).

[21] J. Goldshteyn, "Frequency-resolved ultrafast dynamics of phonon polariton wavepackets in the ferroelectric crystals $LiNbO_3$ and $LiTaO_3$," PhD dissertation (Universität Potsdam, 2015).

[22] Y.-X. Yan and K. A. Nelson, "Impulsive stimulated light scattering. I. General theory," The Journal of Chemical Physics **87**, 6240–6256 (1987).

[23] Y.-X. Yan and K. A. Nelson, "Impulsive stimulated light scattering. II. Comparison to frequency-domain light-scattering spectroscopy," The Journal of Chemical Physics **87**, 6257–6265 (1987).

[24] B. N. Carnio and A. Y. Elezzabi, "A modeling of dispersive tensorial second-order nonlinear effects for the finite-difference time-domain method," Opt. Express **27**, 23432–23445 (2019).

[25] M. Hobden and J. Warner, "The temperature dependence of the refractive indices of pure lithium niobate," Physics Letters **22**, 243–244 (1966).

[26] S. Sanna and W. G. Schmidt, "Lithium niobate X-cut, Y-cut, and Z-cut surfaces from ab initio theory," Phys. Rev. B **81**, 214116 (2010).

[27] N. Iyi, K. Kitamura, F. Izumi, J. Yamamoto, T. Hayashi, H. Asano, and S. Kimura, "Comparative study of defect structures in lithium niobate with different compositions," Journal of Solid State Chemistry **101**, 340–352 (1992).

[28] C. Thierfelder, S. Sanna, A. Schindlmayr, and W. G. Schmidt, "Do we know the band gap of lithium niobate?" physica status solidi c **7**, 362–365 (2010).

[29] D. E. Zelmon, D. L. Small, and D. Jundt, "Infrared corrected Sellmeier coefficients for congruently grown lithium niobate and 5 mol.% magnesium oxide–doped lithium niobate," J. Opt. Soc. Am. B **14**, 3319–3322 (1997).

[30] M. Unferdorben, Z. Szaller, I. Hajdara, J. Hebling, and L. Pálfalvi, "Measurement of Refractive Index and Absorption Coefficient of Congruent and Stoichiometric Lithium Niobate in the Terahertz Range," Journal of Infrared, Millimeter, and Terahertz Waves **36**, 1203–1209 (2015).

[31] H. Lorentz, The Theory of Electrons, note 57 (1923).

[32] J. Colton, Lorentz Oscillator Model of the Dielectric Function, (2020) https://physics.byu.edu/faculty/colton/courses-phy581-fall20.

[33] A. S. Barker and R. Loudon, "Dielectric Properties and Optical Phonons in $LiNbO_3$," Phys. Rev. **158**, 433–445 (1967).

[34] N. Cronin, Microwave and optical waveguides (Institute of Physics Publishing, 1995) Chap. 4.

[35] A. A. Maznev, K. A. Nelson, and J. A. Rogers, "Optical heterodyne detection of laser-induced gratings," Opt. Lett. **23**, 1319–1321 (1998).

[36] H. Pohl, Laser-Induced Dynamic Gratings (Springer, Berlin, Heidelberg, 1986).

[37] A. C. Eckbreth, "BOXCARS: Crossed-beam phase-matched CARS generation in gases," Applied Physics Letters **32**, 421–423 (1978).

[38] J. N. Sweetser, D. N. Fittinghoff, and R. Trebino, "Transient-grating frequency-resolved optical gating," Opt. Lett. **22**, 519–521 (1997).

[39] R. Trebino, K. W. DeLong, D. N. Fittinghoff, J. N. Sweetser, M. A. Krumbügel, B. A. Richman, and D. J. Kane, "Measuring ultrashort laser pulses in the time-frequency domain using frequency-resolved optical gating," Review of Scientific Instruments **68**, 3277–3295 (1997).

[40] B. S. Dastrup, J. R. Hall, and J. A. Johnson, "Experimental determination of the interatomic potential in $LiNbO_3$ via ultrafast lattice control," Applied Physics Letters **110**, 162901 (2017).

[41] D. Kien, J. Loulergue, and J. Etchepare, "Nonlinear response to polariton waves driven in perovskites by femtosecond pulses," Optics Communications **101**, 53–59 (1993).

[42] I. P. Kaminow and W. D. Johnston, "Quantitative Determination of Sources of the Electro-Optic Effect in $LiNbO_3$ and $LiTaO_3$," Phys. Rev. **160**, 519–522 (1967).

[43] H. Inoue, K. Katayama, Q. Shen, T. Toyoda, and K. A. Nelson, "Terahertz reflection response measurement using a phonon polariton wave," Journal of Applied Physics **105**, 054902 (2009).

[44] C. A. Werley, K. A. Nelson, and C. Ryan Tait, "Direct visualization of terahertz electromagnetic waves in classic experimental geometries," American Journal of Physics **80**, 72–81 (2012).

[45] D. W. Ward, E. R. Statz, K. A. Nelson, R. M. Roth, and R. M. Osgood, "Terahertz wave generation and propagation in thin-film lithium niobate produced by crystal ion slicing," Applied Physics Letters **86**, 022908 (2005).

[46] H. J. Bakker, S. Hunsche, and H. Kurz, "Coherent phonon polaritons as probes of anharmonic phonons in ferroelectrics," Rev. Mod. Phys. **70**, 523–536 (1998).

[47] P. Sivarajah, A. Steinbacher, B. Dastrup, J. Lu, M. Xiang, W. Ren, S. Kamba, S. Cao, and K. A. Nelson, "THz-frequency magnon-phonon-polaritons in the collective strong-coupling regime," Journal of Applied Physics **125**, 213103 (2019).

Acknowledgements

Ich bedanke mich in erster Linie bei der udkm-Gruppe unter der Leitung von Prof. Dr. Matias Bargheer, der mir stehts sinnvolle und aufbauende Kommentare bezüglich meiner Arbeit im Labor oder fachlichen Fragen geben konnte. Mein besonderer Dank in der Arbeitsgruppe gilt meinem Betreuer Alexander von Reppert, der mich bei der Fertigstellung dieser Arbeit sehr unterstützte und dessen beeindruckende Arbeitsweise und Motivation mir sehr half. Selten kannte ich eine Autoritätsperson, die ich so respektierte wie ihn und der meine Musiklautstärke derart toleriert.
Dabei möchte ich auch noch Ufo361 danken, ohne dessen inspirierende Musik die Arbeitsstunden nicht so unterhaltsam gewesen wären.
Schlussendlich bedanke ich mich bei meinen FreundInnen, insbesondere meiner WG für die gute Unterhaltung während des Studiums und bei meiner Familie, die mir in diesem für mich persönlich sehr schwierigem Jahr so viel Kraft und Unterstützung gegeben haben, wie man es sich nur wünschen kann.

Declaration

I hereby certify that this thesis has been composed by me and is based on my own work, unless stated otherwise. No other person's work has been used without due acknowledgement in this thesis. All references and verbatim extracts have been quoted, and all sources of information, including graphs and data sets, have been specifically acknowledged.

Date *Signature*